Microwave photonic crystals, graphene, and honeycomb-kagome billiards with threefold symmetry: Comparison with nonrelativistic and relativistic quantum billiards

Weihua Zhang● and Barbara Dietz●*

*Lanzhou Center for Theoretical Physics and the Gansu Provincial Key Laboratory of Theoretical Physics,
Lanzhou University, Lanzhou, Gansu 730000, China*

We present results for properties related to the band structure of a microwave photonic crystal, that is, a flat resonator containing metallic cylinders arranged on a triangular grid, referred to as the Dirac (microwave) billiard, with a threefold-symmetric shape. Such systems have been used to investigate finite-size graphene sheets. It was shown recently that the eigenmodes of rectangular Dirac billiards are well described by the tight-binding model of a finite-size honeycomb-kagome lattice of corresponding shape. We compare properties of the eigenstates of the Dirac billiard with those of the associated graphene and honeycomb-kagome billiard and relativistic quantum billiard. We outline how the eigenstates of threefold-symmetric systems can be separated according to their transformation properties under rotation by $\frac{2\pi}{3}$ into three subspaces, namely singlets, that are rotationally invariant, and doublets that are noninvariant. We reveal for the doublets in graphene and honeycomb-kagome billiards in quasimomentum space a selective excitation of the valley states associated with the two inequivalent Dirac points. For the understanding of symmetry-related features, we extend known results for nonrelativistic quantum billiards and the associated semiclassical approach to relativistic neutrino billiards.

I. INTRODUCTION

We investigate the properties of a microwave photonic crystal consisting of a flat microwave resonator containing metallic cylinders arranged on a triangular grid [1], which has a threefold-symmetric shape. It is shown schematically in Fig. 1. Such resonators have been used to investigate spectral properties of artificial graphene billiards [1–4] and have been named Dirac billiards (DBs). Before constructing the microwave cavity which is cumbersome and needs more than one year, we performed numerical simulations with COMSOL Multiphysics, which are presented in this article. The microwave frequency range is restricted such that only the lowest transverse magnetic modes are excited, implying that the electric-field strength is perpendicular to the top and bottom plate. Then, the system is described by the scalar Helmholtz equation with the Dirichlet boundary condition (BC) that the electric field strength vanishes at the walls of the resonator and cylinders, and is mathematically equivalent to the Schrödinger equation of a quantum billiard of corresponding shape with scatterers at the positions of the cylinders. The voids at the center of, respectively, three cylinders (marked by red and cyan disks in the left lower inset) form a honeycomb structure and, for that arrangement of the metallic cylinders and choice of geometric sizes, the resonance spectrum exhibits two Dirac points framed by van Hove singularities [1–5], independently of the shape of the photonic crystal.

Dirac points are a characteristic of graphene sheets that have attracted a lot of attention [6,7]. They originate from the honeycomb structure [8] which is formed by two interpenetrating triangular sublattices leading to the reduction of the Fermi surface to two independent ones, denoted by $\mathbf{K}_\pm$. There the valence and conduction band touch each other conically, implying that the low-energy excitations exhibit a linear dispersion relation and are governed by Dirac Hamiltonians for massless spin-1/2 quasiparticles, $\hat{H}_\pm = \pm v_F \hat{\boldsymbol{\sigma}} \cdot \boldsymbol{q}$, with $\hat{\boldsymbol{\sigma}} = (\hat{\sigma}_x, \hat{\sigma}_y)$, where $\hat{\sigma}_{x,y,z}$ denote the Pauli matrices and $\boldsymbol{q} = (q_x, q_y)$ the quasimomentum vector. In the vicinity of these valley states graphene features relativistic phenomena [6,7,9–17], which triggered numerous realizations [18] of artificial graphene [19–32]. In order to realize an experimental model for a graphene billiard (GB) with Dirichlet BCs at the sites encircling it, we chose the wall of the DB such that it passes through them; see Fig. 1. It was demonstrated in Refs. [1–5] for rectangular and Africa-shaped Dirac billiards that in the bands of propagating modes framing the lower Dirac point, the DOS and properties of the resonance frequencies and electric-field distributions agree well with those of the eigenvalues and wave functions obtained with a tight-binding model (TBM) for the GB of corresponding shape which takes into account up to third-nearest-neighbor hoppings and wave function overlaps [33]. Previous experiments focused on this Dirac point and the properties of GBs [3] were reproduced; however, the occurrence of a flat band of extraordinarily high spectral density that separates the lower and upper Dirac points and that of the upper one could not be explained with the honeycomb-lattice based TBM. Indeed, it was demonstrated recently that the properties of rectangular DBs are well captured by a TBM for honeycomb-kagome billiards (HBs) whose lattice structure is formed by a honeycomb and kagome sublattice [34–38], which is illustrated in the lower right inset
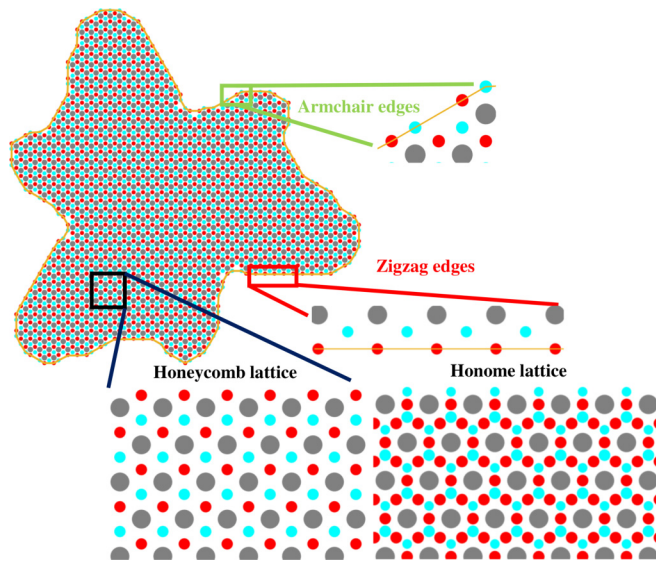
---

*Dietz@lzu.edu.cn

FIG. 1. Design of the DB with threefold symmetry. It contains 1033 metallic cylinders (gray disks) arranged on a triangular grid. The number of voids (red and cyan dots in the lower left inset) formed by respectively three cylinders equals 2066. They are positioned on a honeycomb lattice, which is terminated by zigzag and armchair edges, and correspond to the sites in the graphene billiard. The centers between two adjacent cylinders (red dots in the lower right inset) form a kagome lattice. The electric field strength distribution is localized on both lattices and, consequently, has the structure of a honeycomb-kagome lattice consisting of a honeycomb and a kagome sublattice.

of Fig. 1. We show in the present article that this analogy generally holds for DBs.

With the pioneering fabrication of graphene [6,7,10], interest in relativistic quantum chaos [3–5,14,18,39–47], which entails the study of the spectral properties and properties of the wave functions of GBs [3,4,6,7,39–41,43,44], reemerged. It was shown in Ref. [3] that the spectral properties of DBs and GBs coincide with those of nonrelativistic quantum billiards (QBs) in the vicinity of the band edges, whereas around the Dirac point graphene features relativistic phenomena [1,27,48–50]. If the shape of a QB coincides with that of a classical billiard (CB)—consisting of a bounded two-dimensional domain in which a point particle moves freely and is reflected specularly at the boundary—with a chaotic dynamic, then according to the Bohigas-Giannoni-Schmit conjecture [51–54] the spectral properties coincide with those of random matrices [55] from the Gaussian orthogonal ensemble (GOE) when time-reversal invariance is preserved and with random matrices from the Gaussian unitary ensemble (GUE), when it is violated. Quantum billiards with a threefold-symmetric shape do not comply with this conjecture [56–60]. To be explicit, the eigenstates can be classified according to their transformation properties with respect to rotations by $\frac{2\pi}{3}$ into three subspaces. For one of these subspaces the eigenstates are invariant under this transformation. The eigenfunctions of the other two subspaces are complex, the associated subspectra are degenerate, and the fluctuation properties coincide with those of random matrices

from the GUE if the shape has no further geometric symmetry, even though time-reversal invariance is preserved. These discrepancies could be explained on the basis of a semiclassical approach [61–67]. In Refs. [63,67] symmetry-projected trace formulas were derived for the spectral density of the subspectra, which involve in addition to the full-system periodic orbits pseudo-orbits, which are periodic orbits only in the symmetry-projected fundamental domains. The direct link between the quantum spectral density and classical periodic orbits is best visualized by length spectra, obtained from the Fourier transform of the spectral density from wave number to length, which exhibit peaks at the lengths of periodic orbits. In Refs. [3,38] length spectra of DBs and the associated GBs and HBs were shown to agree well with those of the QB in the vicinity of the band edges. We will address the question of whether this analogy also holds for the pseudo-orbits.

In 1987 Berry and Mondragon proposed relativistic neutrino billiards [68] (NBs) that are governed by the Dirac equation for a spin-1/2 particle, which is confined to the billiard domain by imposing appropriate BCs. The associated Dirac Hamiltonian is not invariant under time reversal, so the spectral properties of NBs with the shape of a chaotic CB typically coincide with those of random matrices from the GUE, if the shape has no additional geometric symmetry. The spectral properties of GBs were expected to be similar to those of NBs in the valley regions around the $\mathbf{K}_{\pm}$ points, because there they are governed by the same wave equations. Indeed, experiments with graphene quantum dots with the shape of a chaotic Africa billiard yielded that the spectral properties follow GUE statistics [14]. However, tight-binding model (TBM) calculations [43] and experimental investigations [1,2] with GBs of that shape revealed that they coincide with those of random matrices from the GOE. The discrepancies were attributed to the differing conditions on the wave functions along the boundary [41,45,46]. In a finite-size graphene sheet or GB waves are scattered back at the boundary, leading to a mixing of the $\mathbf{K}_{\pm}$ valley states and thus to a coupling of the Dirac Hamiltonians $\hat{H}_{\pm}$. The resulting four-dimensional Dirac equation preserves time-reversal invariance.

In the present article we compare the spectral properties and length spectra deduced from the spectra of DBs, GBs, and HBs around the Dirac points with those of massless and massive NBs. Their eigenvalues and wave functions are obtained from a boundary-integral equation (BIE) which has been deduced based on Green's theorem for massless NBs in Ref. [68] and extended to massive NBs in Ref. [69]. With increasing mass, NBs undergo a transition from the ultrarelativistic to the nonrelativistic limit [69–72]. Based on the BIEs for massive NBs trace formulas were derived for their spectral density which capture that transition [69]. Like in the nonrelativistic case, the eigenstates of NBs with a threefold-symmetric shape can be classified according to their transformation properties under rotation by $\frac{2\pi}{3}$. We will outline how the BIE can be separated into three symmetry-projected BIEs. Using the trace formula for massive NBs we derive symmetry-projected trace formulas that are employed to understand their length spectra obtained from the Fourier transform of the symmetry-projected spectral density. Note that NBs and, generally, relativistic QBs have no well-defined classical limit; however, the trace formula provides a direct

link to the classical dynamics [73,74]. Similarly, a trace formula was derived for the relativistic region of GBs [75]. In Ref. [44] a trace formula was obtained for GBs with infinite-mass confinement which was shown in Ref. [69] to coincide with that of massless NBs. We compare length spectra involving all eigenvalues and symmetry-projected subspectra of the NBs with the corresponding ones of the DBs, GBs, and HBs to test to what extent this analogy holds.

The investigation of the fluctuation properties in the symmetry-projected subspectra is also interesting from another point of view. Actually, a motivation for the investigation of properties of DBs with threefold symmetry comes from experiments which were performed in the context of topological phononics and valleytronics with open phononic and sonic crystals that are composed of rods with triangular cross sections arranged on a triangular grid [76–80]. Depending on the orientation of the rods, these systems may exhibit C_3 or C_{3v} symmetry and may lead to a selective excitation of the valley-vortex states resulting in topological phenomena related to pseudospin-dependent transport. Similarly, we reveal for the degenerate eigenstates of the GB and HB a selective excitation of the valley states associated with the $\mathbf{K}_\pm$ points, as outlined in Sec. IV, after subdividing into the three symmetry-projected subspaces, implying that there backscattering at the boundary does not lead to a mixing of the valley states [41]. As explained above, the discrepancies between the spectral properties of DBs, GBs, and HBs in the vicinity of the Dirac points and NBs have been attributed to the backscattering. Therefore, the question arises of whether these are lifted due to the selectivity. To find out, we compare their spectral properties which, actually, are expected to be GUE for all cases, and their length spectra.

Section II is divided into several subsections. In Sec. II A we review the properties of quantum systems with threefold symmetry and in Sec. II B the results for nonrelativistic quantum billiards. In Sec. II C we extend these results to relativistic QBs, namely massless and massive NBs and then compare in Sec. II D the spectral properties of QBs and NBs. In Sec. II E we extend the semiclassical theory [61,62] for threefold symmetric QBs [63] to NBs for an understanding of the symmetry-projected length spectra. The derivation is based on the trace formula for massive NBs [69]. In Secs. III and IV we present the results for the DB, the GB, and the HB, which are discussed in Sec. V.

II. NONRELATIVISTIC AND RELATIVISTIC QUANTUM BILLIARDS WITH THREEFOLD SYMMETRY

A. Quantum systems with threefold symmetry

First we consider nonrelativistic quantum systems subject to a potential with C_3 symmetry, which we realize with quantum billiards of which the shape has a threefold rotational symmetry. Motivation for the choice of the shape stems from experiments which were performed 20 years ago with a superconducting microwave billiard to investigate the spectral properties of quantum systems with C_3 symmetry. Its shape is shown schematically in Fig. 2. The domain Ω of the billiard is defined in the (x, y) plane by the
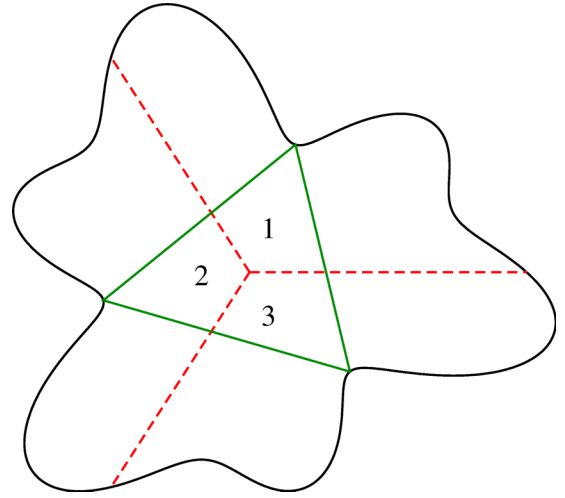

FIG. 2. Shape of the threefold-symmetric billiard. The billiard domain can be divided into three fundamental domains that are mapped onto each other under rotation by $\frac{2\pi}{3}$. A possible subdivision is indicated by the red-dashed lines. Any other partition can be obtained by rotation of the lines. The shortest connected PO (green lines) has a length of $\tilde{l}_s = 11.336 r_0/3$.

parametrization

$$x(r, \phi) + iy(r, \phi) = w(r, \phi) = R(r, \phi)e^{i\phi},$$
$$\phi \in [0, 2\pi), \quad r = [0, r_0], \quad (1)$$

with

$$R(r, \phi) = rf(\phi), \quad (2)$$

$$f(\phi) = 1 + 0.2 \cos(3\phi) - 0.2 \sin(6\phi). \quad (3)$$

The boundary $\partial\Omega$ of the billiard is defined by $w(r = r_0, \phi)$ where we chose $r_0 = 3$ in the numerical simulations. The shape is threefold symmetric, and thus can be divided into three fundamental domains which can be mapped onto each other by a rotation by $\frac{2\pi}{3}$. This symmetry property is imprinted on the wave functions $\psi(r, \phi)$, which are governed by the Schrödinger equation or, equivalently, the scalar Helmholtz equation, with Dirichlet BCs along the boundary of the QB,

$$\hat{H}\psi_m(r, \phi) = -\Delta_{(r,\phi)}\psi_m(r, \phi) = k_m^2 \psi_m(r, \phi),$$
$$\psi_m(r = r_0, \phi) = 0. \quad (4)$$

The eigenenergies $E_m = k_m^2$ of the Hamiltonian $\hat{H} = -\Delta_{(r,\phi)}$ are given in terms of the wave numbers k_m, which are related to the eigenfrequencies ν_m of the corresponding microwave billiard through the relation $k_m = 2\pi\nu_m/c$, where c denotes the velocity of light in vacuum. For the parametrization Eq. (2) the gradient $\boldsymbol{\nabla}_{(x,y)} = (\frac{\partial}{\partial x}, \frac{\partial}{\partial y})$ is obtained from [81]

$$\left(\frac{\partial}{\partial x} + i\frac{\partial}{\partial y}\right) = J\left\{-i\frac{\partial w(r, \phi)}{\partial\phi}\frac{\partial}{\partial r} + i\frac{\partial w(r, \phi)}{\partial r}\frac{\partial}{\partial\phi}\right\},$$
$$J = \left(R(r, \phi)\frac{\partial R(r, \phi)}{\partial r}\right)^{-1}, \quad (5)$$

yielding for the Laplace operator $\Delta_{(x,y)} = \frac{\partial^2}{\partial x^2} + \frac{\partial^2}{\partial y^2}$ in polar coordinates (r, ϕ),

$$
\begin{aligned}
J^{-2}\Delta_{(r,\phi)} = r^2 & \left\{ \left(\frac{\partial f}{\partial \phi}\right)^2 + f^2 \right\} \frac{\partial^2}{\partial r^2} + f^2 \frac{\partial^2}{\partial \phi^2} \\
& - 2rf\left(\frac{\partial f}{\partial \phi}\right)\frac{\partial^2}{\partial r \partial \phi} + \left\{ 2r\left(\frac{\partial f}{\partial \phi}\right)^2 + rf^2 \right. \\
& \left. - rf\left(\frac{\partial^2 f}{\partial \phi^2}\right) \right\} \frac{\partial}{\partial r}.
\end{aligned}
\tag{6}
$$

The solutions of the free-space Schrödinger equation can be written in terms of an expansion of the Bessel functions $J_m(x)$ [81],

$$
\psi(r,\phi) = \sum_m J_m(kR(r,\phi))[a_m \cos(m\phi) + b_m \sin(m\phi)]. \tag{7}
$$

For quantum systems with threefold symmetry the symmetry group is given by $\boldsymbol{G} = C_3 = \{\boldsymbol{e}, \boldsymbol{g}, \boldsymbol{g}^2\}$, where $\boldsymbol{e}$ is the identity operation and $\boldsymbol{g}$ denotes rotation by $\frac{2\pi}{3}$. The symmetry group C_3 has three one-dimensional irreducible representations labeled by $l = 0, 1, 2$, which are given by $\mathcal{M}^{(l)}(\boldsymbol{g}^\lambda) = e^{il\lambda\frac{2l\pi}{3}}$ with λ taking either of the values $\{0, 1, 2\}$. Consequently, the solutions of the wave equation (4) can be separated into three subspaces which are defined by the transformation properties of the associated eigenfunctions $\psi_m^{(l)}(r, \phi)$ under rotation by $\frac{2\lambda\pi}{3}$, $\lambda = 0, 1, 2$ when applying the rotation operator [56,57,59,67]

$$
\hat{U}(\boldsymbol{g}) = \hat{R} = e^{i\frac{2\pi}{3}\hat{L}} \tag{8}
$$

with $\hat{L}$ denoting the angular momentum operator,

$$
\begin{aligned}
\hat{U}(\boldsymbol{g}^\lambda)\psi_m^{(l)}(r, \phi) &= \hat{R}^\lambda \psi_m^{(l)}(r, \phi) \\
&= \psi_m^{(l)}(\boldsymbol{g}^{-\lambda}[\boldsymbol{r}]) = \psi_m^{(l)}\left(r, \phi - \frac{2\pi}{3}\lambda\right) \\
&= e^{i\frac{2l\pi}{3}\lambda}\psi_m^{(l)}(r, \phi), \tag{9}
\end{aligned}
$$

where

$$
[\hat{R}, \hat{H}] = 0. \tag{10}
$$

The projection operator $\hat{P}_l$ onto the irreducible subspace labeled with l, which is defined by the properties $\hat{P}_l \psi^{(l')}(r, \phi) = \delta_{ll'}\psi^{(l')}(r, \phi)$ and $\hat{P}_l^2 = \hat{P}_l$, is given by

$$
\hat{P}_l = \frac{1}{3}\sum_{\lambda=0}^{2} \chi_l(\boldsymbol{g}^\lambda)\hat{U}^\dagger(\boldsymbol{g}^\lambda), \tag{11}
$$

where $\chi_l(\boldsymbol{g}) = \mathrm{tr}\mathcal{M}^{(l)}(\boldsymbol{g})$ denotes the character of the corresponding irreducible representation.

For $l = 0$ the wave functions are invariant under rotation by $\frac{2\pi}{3}$, whereas for $l = 1, 2$, $\hat{R}$ needs to be applied three times on $\psi_m^{(l)}(r, \phi)$ in order to recover its initial value. The wave functions are real for $l = 0$ and invariant under application of the antiunitary time-reversal operator $\hat{T} = \hat{K}$ with $\hat{K}$ the complex conjugation operator [82], whereas with $\psi_m^{(l)*}(r, \phi - \frac{2\pi}{3}) = e^{-i\frac{2l\pi}{3}}\psi_m^{(l)*}(r, \phi)$,

$$
\hat{T}\psi_m^{(1,2)}(r, \phi) = \left[\psi_m^{(1,2)}(r, \phi)\right]^* = \psi_m^{(2,1)}(r, \phi). \tag{12}
$$

However, the QB itself is invariant under time reversal,

$$
[\hat{H}, \hat{T}] = 0, \tag{13}
$$

implying that $\psi_m^{(1,2)}(r, \phi)$ and $\hat{T}\psi_m^{(1,2)}(r, \phi) = \psi_m^{(2,1)}(r, \phi)$ are eigenfunctions to the same eigenvalue k_m^2. Thus, the eigenvalue spectrum can be separated into nondegenerate eigenvalues (singlets) and pairwise degenerate ones (doublets). Note that due to the degeneracy of the eigenvalues a complete set of real eigenfunctions of $\hat{H}$ corresponding to that eigenvalue can be constructed from a linear combination of $\psi_m^{(1)}(r, \phi)$ and $\psi_m^{(2)}(r, \phi)$. As a consequence of the behavior of the eigenstates of the QBs with threefold symmetry under the $\hat{T}$ operation, the spectral properties of the singlets follow GOE statistics, while those of the two doublet partners exhibit GUE statistics, if the dynamic of the corresponding CB is chaotic. This is generally the case for QBs with C_3 symmetry and no mirror symmetry [83,84] and was confirmed experimentally in high-precision experiments with superconducting [59,60] and normal conducting [83] microwave billiards. If the spectra of quantum systems with C_3 symmetry and a chaotic classical dynamics are not separated according to their symmetry properties, their fluctuation properties coincide with those of a superposition of one random matrix from the GOE and two of same dimension from the GUE with identical eigenvalues and eigenvectors related through Eq. (12).

B. Nonrelativistic quantum billiards

In Ref. [84] the experimental results were validated numerically with a procedure which is based on the finite-element method (FEM). In the present paper we use BIEs originating from the Green theorem, which take into account the BCs and thus provide an exact integral equation for the eigenvalues and the associated eigenfunctions of QBs [85]. Another advantage with respect to the FEM is that the eigenvalue problem is reduced from discretization of the two-dimensional billiard area required for the FEM to that of the boundary. To further reduce the numerical effort we incorporate the symmetry properties into the BIE and thereby obtain individual BIEs for each subspace with the boundary integrals reduced to one-third of the boundary.

To obtain the eigenvalues of the QB we have to solve the interior Dirichlet problem. Then, the eigenvalues are obtained from a Fredholm equation of the second kind [85] which involves the normal derivative $u(s) = \partial_n \psi(s)$ instead of the wave function $\psi(s)$, where s denotes the arclength parameter

$$
s(\phi) = \int_0^\phi |w'(\tilde{\phi})|d\tilde{\phi}, \; s \in [0, \mathcal{L}), \; ds = |w'(\phi)|d\phi \tag{14}
$$

with $w'(\phi) = \frac{dw(\phi)}{d\phi}$ and $\mathcal{L}$ the perimeter,

$$
\begin{aligned}
u(s') &= -2\oint_{\partial\Omega} ds\,\partial_{n'}G_0[k; \boldsymbol{r}(s'), \boldsymbol{r}(s)]u(s) \\
&= \hat{Q}^{QB}(k)u(s). \tag{15}
\end{aligned}
$$

Here,

$$
G_0[k; \boldsymbol{r}(s'), \boldsymbol{r}(s)] = -\frac{i}{4}H_0^{(1)}(k|\boldsymbol{r} - \boldsymbol{r}'|) \tag{16}
$$

is the two-dimensional free-space Green function and $H_m^{(1)}(k\rho) = J_m(k\rho) + iY_m(k\rho)$ refers to the Hankel function of the first kind of order m [86]. Denoting by $\alpha(s)$ the angle of the outward-pointing normal vector $\boldsymbol{n}(s)$ with respect to the x axis, i.e., $\boldsymbol{n}(s) = [\cos\alpha(s), \sin\alpha(s)]$, the distance between the boundary points at s and s' by $\rho = |\boldsymbol{r}(s) - \boldsymbol{r}(s')|$, and by $\xi(s, s')$ the angle between $\boldsymbol{\rho}(s, s') = \boldsymbol{r}(s) - \boldsymbol{r}(s')$ and the x axis, the normal derivative equals

$$\partial_{n'} G_0[k; \boldsymbol{r}(s'), \boldsymbol{r}(s)] \tag{17}$$

$$= \boldsymbol{n}(s') \cdot \frac{\boldsymbol{r}(s) - \boldsymbol{r}(s')}{|\boldsymbol{r}(s) - \boldsymbol{r}(s')|}\left(-\frac{i}{4}k\right)H_1^{(1)}(k\rho)$$

$$= \cos\left[\alpha(s') - \xi(s, s')\right]\left(-\frac{i}{4}k\right)H_1^{(1)}(k\rho). \tag{18}$$

Accordingly, the BIE Eq. (15) can be cast into the form [85]

$$u(\phi') = \int_0^{2\pi} d\phi |w'(\phi)| Q^{QB}(k; \phi, \phi') u(\phi), \tag{19}$$

$$Q^{QB}(k; \phi, \phi') = i\frac{k}{2}\cos\left[\alpha(\phi') - \xi(\phi, \phi')\right]H_1^{(1)}(k\rho). \tag{20}$$

To take into account the threefold symmetry of the QB we use periodicity properties resulting from it,

$$w\left(\phi + \lambda\frac{2\pi}{3}\right) = e^{i\lambda\frac{2\pi}{3}}w(\phi), \tag{21}$$

$$w'\left(\phi + \lambda\frac{2\pi}{3}\right) = e^{i\lambda\frac{2\pi}{3}}w'(\phi), \tag{22}$$

$$e^{i\alpha(\phi + \lambda\frac{2\pi}{3})} = e^{i\lambda\frac{2\pi}{3}}e^{i\alpha(\phi)}, \tag{23}$$

with $\lambda = 0, 1, 2$ yielding that

$$Q^{QB}\left(k; \phi, \phi' - \lambda\frac{2\pi}{3}\right) = Q^{QB}\left(k; \phi + \lambda\frac{2\pi}{3}, \phi'\right). \tag{24}$$

Restricting ϕ to $\phi \in [0, \frac{2\pi}{3})$ and introducing wave functions for the three domains marked by $\lambda = 0, 1, 2$ in Fig. 2, $\psi_\lambda(\phi) = \psi(\phi + \lambda\frac{2\pi}{3})$, $u_\lambda(\phi) = \partial_n\psi_\lambda(\phi)$, and

$$M_\lambda^{QB}(k; \phi, \phi') = Q^{QB}\left(k; \phi + \lambda\frac{2\pi}{3}, \phi'\right), \tag{25}$$

the BIE becomes

$$\boldsymbol{u}(\phi') = \int_0^{\frac{2\pi}{3}} d\phi \hat{M}^{QB}(k; \phi, \phi') \boldsymbol{u}(\phi) \tag{26}$$

with

$$\boldsymbol{u}(\phi) = \begin{pmatrix} u_0 \\ u_1 \\ u_2 \end{pmatrix}(\phi), \tag{27}$$

$$\hat{M}^{QB}(k; \phi, \phi') = \begin{pmatrix} M_0^{QB} & M_1^{QB} & M_2^{QB} \\ M_2^{QB} & M_0^{QB} & M_1^{QB} \\ M_1^{QB} & M_2^{QB} & M_0^{QB} \end{pmatrix}(k; \phi, \phi'). \tag{28}$$

This procedure corresponds to a separation of phase space into fundamental domains to which all group operations are applied in order to generate the whole phase space [63]. On

multiplication with

$$\hat{U} = \frac{1}{\sqrt{3}}\begin{pmatrix} 1 & e^{i\frac{4\pi}{3}} & e^{i\frac{4\pi}{3}} \\ 1 & 1 & e^{i\frac{2\pi}{3}} \\ 1 & e^{i\frac{2\pi}{3}} & 1 \end{pmatrix}, \tag{29}$$

$\hat{M}^{QB}(k; \phi, \phi')$ is brought to diagonal form,

$$[\hat{U}^\dagger\hat{M}^{QB}(k; \phi, \phi')\hat{U}]_{lm} = \tilde{M}^{QB(l)}(k; \phi, \phi')\delta_{lm}, \tag{30}$$

yielding three independent symmetry-projected BIEs,

$$u^{(l)}(\phi') = \int_0^{\frac{2\pi}{3}} d\phi \tilde{M}^{QB(l)}(k; \phi, \phi') u^{(l)}(\phi), \tag{31}$$

where $u^{(l)}(\phi) = \partial_n\psi^{(l)}(\phi)$, $l = 0, 1, 2$, and

$$\tilde{M}^{QB(l)}(k; \phi, \phi') = \sum_{\lambda=0}^2 e^{i\frac{2l\pi}{3}\lambda} M_\lambda^{QB}(k; \phi, \phi'). \tag{32}$$

Note that the prefactor of M_λ^{QB} corresponds to the character $\chi_l(\boldsymbol{g}^\lambda) = e^{i\frac{2l\pi}{3}\lambda}$ of the representation matrix $\mathcal{M}^{(l)}(\boldsymbol{g}^\lambda)$. The BIEs Eq. (31) have solutions only for discrete values of k yielding the eigenvalues k_m^2, $m = 1, 2, \ldots$, of the QB for the three subspectra corresponding to the irreducible representations of C_3. The eigenvalues corresponding to the rotationally invariant states $l = 0$ are nondegenerate, whereas for $l = 1, 2$ they form doublets of degenerate ones.

C. Relativistic quantum billiards

The Dirac equation for a free spin-1/2 particle of mass m moving with momentum $\hat{\boldsymbol{p}} = -i\hbar\boldsymbol{\nabla}$ in the two-dimensional $\boldsymbol{r} = (x, y)$ plane is given by

$$\hat{H}_D\boldsymbol{\psi} = (c\hat{\boldsymbol{\sigma}}\cdot\hat{\boldsymbol{p}} + mc^2\hat{\sigma}_z)\boldsymbol{\psi} = E\boldsymbol{\psi}, \quad \boldsymbol{\psi} = \begin{pmatrix}\psi_1 \\ \psi_2\end{pmatrix}. \tag{33}$$

Here, $\hat{\boldsymbol{\sigma}} = (\hat{\sigma}_x, \hat{\sigma}_y)$, $\hat{\sigma}_{x,y,z}$ are the Pauli matrices, and $E = \hbar c k_E = \hbar c k\sqrt{1 + \beta^2}$ is the energy of the particle, where k is the free-space wave vector and $\beta = \frac{mc}{\hbar k}$ is the ratio of the rest-energy momentum and free-space momentum. The particle is confined to the billiard domain Ω by requiring that the Hamiltonian of a closed system should preserve self-adjointness [68], that is, that there is no outgoing flow, thus yielding the BC

$$\psi_2(s) = ie^{i\alpha(s)}\psi_1(s), \tag{34}$$

which imposes a phase relation on the wave-function components $\psi_{1,2}(s)$ along the boundary $\partial\Omega$. Introducing local coordinates (n, s) in the directions of $\boldsymbol{n}(s)$ and of the tangential vector $\boldsymbol{t}(s) = [-\sin\alpha(s), \cos\alpha(s)]$ at $\boldsymbol{r}(s)$ with $n = 0$ on the boundary, this BC can be turned into separate ones for the two wave-function components,

$$(\partial_n + i\partial_s)\psi_1(n, s)|_{n\to 0^-} = -k\mathcal{K}^{-1}\psi_1(s),$$
$$(\partial_n - i\partial_s)\psi_2(n, s)|_{n\to 0^-} = k\mathcal{K}\psi_2(s). \tag{35}$$

Here, $\partial_n = \boldsymbol{n}\cdot\boldsymbol{\nabla}$ and $\partial_s = \boldsymbol{t}\cdot\boldsymbol{\nabla}$ denote the normal and tangential derivatives along $\partial\Omega$, respectively, yielding $\partial_x \pm i\partial_y = e^{\pm i\alpha(s)}(\partial_n \pm i\partial_s)$, $n\to 0^-$ means that the boundary is

approached in the direction of $\boldsymbol{n}(s)$ from the interior, and $\psi_{1,2}(n=0,s) = \psi_{1,2}(s)$. Furthermore, we introduced

$$\mathcal{K} = \sqrt{\frac{1-\sin\theta_\beta}{1+\sin\theta_\beta}}, \quad (36)$$

$$\cos\theta_\beta = \frac{1}{\sqrt{1+\beta^2}}, \quad \sin\theta_\beta = \frac{\beta}{\sqrt{1+\beta^2}}. \quad (37)$$

The nonrelativistic limit is reached when the energy is close to the rest energy, $E \simeq mc^2$, which is reached in the limit $\beta = \frac{mc}{\hbar k} \to \infty$ for fixed, nonzero $\hbar k$, i.e., in a given k-value range for $\tilde{\beta} = \frac{mc}{\hbar} \to \infty$ [70], where $\tilde{\beta}$ denotes the rest-energy momentum mc in units of $\hbar$. In that limit $\mathcal{K} \simeq \frac{1}{2\beta} \to 0$ and $\theta_\beta \to \pi/2$. We demonstrated in Ref. [69] that the nonrelativistic limit complies with the BCs for massive NBs yielding that for sufficiently large $\tilde{\beta}$ the spinor components decouple and their wave equations coincide with those of QBs subject to Robin BCs that eventually turn into Dirichlet BCs with increasing $\tilde{\beta}$.

Introducing a two-component spinor $\tilde{\boldsymbol{\psi}}(\boldsymbol{r})$ which is obtained by dividing the components $\psi_{1,2}(\boldsymbol{r})$ in Eq. (33) by the amplitudes of the corresponding free-space wave-function components [70],

$$\begin{pmatrix} \psi_1 \\ \psi_2 \end{pmatrix} = \begin{pmatrix} \sqrt{\frac{1+\sin\theta_\beta}{2}}\tilde{\psi}_1 \\ \sqrt{\frac{1-\sin\theta_\beta}{2}}\tilde{\psi}_2 \end{pmatrix}, \quad (38)$$

leads to a Dirac equation of massive NBs

$$k\tilde{\boldsymbol{\psi}}(\boldsymbol{r}) + i\hat{\boldsymbol{\sigma}} \cdot \nabla\tilde{\boldsymbol{\psi}}(\boldsymbol{r}) = 0, \quad (39)$$

$$\tilde{\psi}_2(s) = ie^{i\alpha(s)}\mathcal{K}^{-1}\tilde{\psi}_1(s), \quad (40)$$

which has the same form as for the massless NB [68] with modified BCs that approach for $\tilde{\beta} \to 0$ those for massless NBs given in Eq. (34).

Application of Green's theorem yields BIEs which contain singularities originating from the logarithmic singularity of $H_0(k\rho)$ and the $1/\rho$ singularity of $H_1(k\rho)$ for $\rho = 0$. In Ref. [68] these singularities could be removed for massless neutrinos by using a combination of the BIEs for the two wave-function components $\psi_{1,2}(\phi)$ and applying the BC. Due to the modified BCs the derivation of BIEs containing no singularities is more involved for nonzero m [69]. The BIEs for the two wave-function components can be written in a form similar to that for the QB given in Eq. (19),

$$\tilde{\boldsymbol{\psi}}^\dagger[\boldsymbol{r}(\phi')]$$
$$= \oint_{\partial\Omega} d\phi|w'(\phi)|e^{i\frac{\Delta\Phi(\phi,\phi')}{2}}\hat{Q}^{NB}[k;\boldsymbol{r}(\phi'),\boldsymbol{r}(\phi)]\tilde{\boldsymbol{\psi}}^\dagger[\boldsymbol{r}(\phi)]$$
$$= \hat{\boldsymbol{Q}}^{NB}(k)\tilde{\boldsymbol{\psi}}^\dagger[\boldsymbol{r}(\phi)], \quad (41)$$

with $\Delta\Phi(\phi,\phi') = \frac{\alpha(\phi')-\alpha(\phi)}{2}$ and $\hat{\boldsymbol{Q}}_{ij}^{NB}(k) = \hat{\boldsymbol{Q}}_j^{NB}(k)\delta_{ij}$, and $\hat{\boldsymbol{Q}}_j^{NB}(k)$ denoting the integral operator which is applied to $\tilde{\psi}_j^*(\phi)$ to obtain $\tilde{\psi}_j^*(\phi')$. For the first component the BIE is

given by

$$\tilde{\psi}_1^*(\phi') = \int_0^{2\pi} d\phi|w'(\phi)|e^{i\frac{\Delta\Phi(\phi,\phi')}{2}}Q_1^{NB}(k;\phi,\phi')\tilde{\psi}_1^*(\phi), \quad (42)$$
$$Q_1^{NB}(k;\phi,\phi')$$
$$= i\frac{k}{2}\left\{i\cos\theta_\beta \sin\left(\frac{\Delta\Phi(\phi,\phi')}{2}\right)H_0^{(1)}(k\rho)\right.$$
$$+ i\sin\theta_\beta \sin\left(\frac{\alpha(\phi')+\alpha(\phi)}{2}-\xi(\phi,\phi')\right)H_1^{(1)}(k\rho)$$
$$\left.+ \cos\left(\frac{\alpha(\phi')+\alpha(\phi)}{2}-\xi(\phi,\phi')\right)H_1^{(1)}(k\rho)\right\}. \quad (43)$$

In the sequel we suppress the argument of $\rho = \rho(\phi,\phi')$. For $\phi \to \phi'$ the first and the last term vanish [87] whereas the second term approaches[1]

$$Q_1^{NB}(k;\phi,\phi')ds \xrightarrow{\phi\to\phi'} -\frac{\sin\theta_\beta}{2\pi}[\kappa(s)ds + 2i]. \quad (44)$$

The corresponding equation for $\tilde{\psi}_2^*(\phi')$ is deduced from Eq. (40) by multiplying the integrand with $e^{-i\Delta\Phi(\phi,\phi')}$. The ultrarelativistic and nonrelativistic cases are attained for $\theta_\beta = 0$ and $\theta_\beta = \frac{\pi}{2}$, respectively. The corresponding BIEs for the wave-function components $\psi_{1,2}$ are obtained from $\tilde{\psi}_{1,2}$ by employing Eq. (38).

Before implementing the symmetry properties in the BIEs for NBs a few remarks are necessary. For a QB of which the shape exhibits mirror symmetries the wave functions are either symmetric or antisymmetric with respect to the symmetry axis; that is, they follow Neumann, respectively, Dirichlet BCs along this axis. This, however, is not the case for the corresponding NB, because the wave functions, obtained by applying the associated symmetry operation to those of the full system, do not obey the BC Eq. (40) for finite values of $\tilde{\beta}$. If, on the other hand, the billiard shape has an N-fold rotational symmetry, $w(z') = e^{il\frac{2\pi}{N}}w(z)$ and $e^{i\alpha(z')} = e^{il\frac{2\pi}{N}}e^{i\alpha(z)}$ with $z' = e^{il\frac{2\pi}{N}}z$, $l = 1, \ldots, N-1$, then the free-space solution of the transformed Hamiltonian $\hat{\boldsymbol{H}}_D(z') = \hat{\boldsymbol{U}}^\dagger\hat{\boldsymbol{H}}_D\hat{\boldsymbol{U}}$ with $\hat{\boldsymbol{H}}_D$ defined in Eq. (33) and

$$\hat{\boldsymbol{U}} = \begin{pmatrix} e^{il\frac{\pi}{N}} & 0 \\ 0 & e^{-il\frac{\pi}{N}} \end{pmatrix}, \quad (45)$$

$\boldsymbol{\psi}' = \hat{\boldsymbol{U}}^\dagger\boldsymbol{\psi}$, obeys the BC Eq. (34) if the original wave function $\boldsymbol{\psi}(z)$ does [87]. The Hamiltonian of NBs with N-fold rotational symmetry can be brought to a block-diagonal structure with each of the N blocks corresponding to one of the irreducible representations of the symmetry group, defined by the transformation properties of the associated eigenstates with respect to a rotation by $l\frac{2\pi}{N}$, $l = 0, 1, \ldots, N-1$ [87,88], where in the case considered here $N = 3$. Indeed, the integrand $Q_1^{NB}(k;\phi,\phi')$ of Eq. (41) exhibits the same periodicity

_____

[1]This term results from a more accurate determination of $e^{i\xi(\phi'+\delta\phi',\phi')}$ for $\phi \to \phi'$ than in Ref. [69], where it was based on the estimate given below Eq. (41) of Ref. [87] obtained by neglecting terms of second and higher order in $\delta\phi'$ in the Taylor expansion of $\rho(\phi' + \delta\phi')$, which is sufficient to show that the first and last terms in Eq. (43) vanish.

as $Q^{QB}(k; \phi, \phi')$ given in Eq. (24),

$$Q_1^{NB}\left(k; \phi, \phi' + \lambda \frac{2\pi}{3}\right) = Q_1^{NB}\left(k; \phi - \lambda \frac{2\pi}{3}, \phi'\right) \quad (46)$$

with $\lambda = 0, 1, 2$, so we may proceed as in Eqs. (24)–(32) to separate the BIE Eq. (41) into individual ones for the three irreducible representations of C_3,

$$\tilde{\psi}_1^{(l)*}(\phi') = \int_0^{\frac{2\pi}{3}} d\phi \tilde{M}^{NB(l)}(k; \phi, \phi') \tilde{\psi}_1^{(l)*}(\phi) \quad (47)$$

with $l = 0, 1, 2$ and [63]

$$\tilde{M}_1^{NB(l)}(k; \phi, \phi') = \sum_{\lambda=0}^{2} e^{i\frac{2l\pi}{3}\lambda} M_{1,\lambda}^{NB}(k; \phi, \phi'), \quad (48)$$

where

$$M_{1,\lambda}^{NB}(k; \phi, \phi') = Q_1^{NB}\left(k; \phi + \lambda \frac{2\pi}{3}, \phi'\right). \quad (49)$$

Note that the Dirac Hamiltonian Eq. (33) does not commute with the time-reversal operator $\hat{T}$. Consequently, if the shape has no mirror symmetry, the eigenvalues corresponding to the invariant representations of C_3 labeled by $l = 1, 2$ are not degenerate and also for the singlets the spectral properties of massless NBs typically coincide with those of the GUE if the shape of the billiard generates a chaotic classical dynamics. Furthermore, the BCs Eq. (34) or, equivalently, Eq. (40) relate wave function components to each other which belong to different representations l. Namely, using that $\psi_2^{(l)}(\phi - \frac{2\pi}{3}) = e^{i\frac{2l\pi}{3}} \psi_2^{(l)}(\phi)$ and Eq. (23) supposing that with Eq. (34) $\psi_1^{(l')}(\phi) = ie^{i\alpha(\phi)} \psi_2^{(l)}(\phi)$ yields

$$\psi_1^{(l')}\left(\phi - \frac{2\pi}{3}\right) = ie^{\alpha(\phi - \frac{2\pi}{3})} \psi_2^{(l)}\left(\phi - \frac{2\pi}{3}\right)$$
$$= ie^{-i\frac{2\pi}{3}} e^{\alpha(\phi)} e^{i\frac{2l\pi}{3}} \psi_2^{(l)}(\phi)$$
$$= e^{i\frac{2(l-1)\pi}{3}} \psi_1^{(l')}(\phi), \quad (50)$$

i.e., $l' = l - 1$, where $l = -1$ is equivalent to $l = 2$.

D. Spectral properties of quantum and neutrino billiards

Based on the BIEs Eqs. (32) and (48) we computed 3000 eigenvalues and corresponding wave functions for each symmetry class for the QB and the massless NB and 2000 for NBs with mass $\tilde{\beta} = 2, 20, 100$. In Fig. 3 we show examples for the intensity distributions of the wave functions of the QB for the singlets (left three columns) and only for one of the doublet partners (right three columns), because for the other one they are the same. They were obtained by employing the BIEs deduced on the basis of Green's theorem for QBs [85]. The nodal domain structure is blurry for the doublets, because the corresponding wave functions are complex. In Figs. 4–6 we exhibit wave function intensity distributions of NBs for the eigenstates with $n = 45, 48, 106$ which were computed using the BIEs for massive NBs [69]. They are shown for the first and second component of the singlets (first and second column), and of the doublets with $l = 1$ (third and fourth column) and $l = 2$ (fifth and sixth column) for $\tilde{\beta} = 0$ (first row), $\tilde{\beta} = 20$ (second row), and $\tilde{\beta} = 100$ (third row). In all cases the
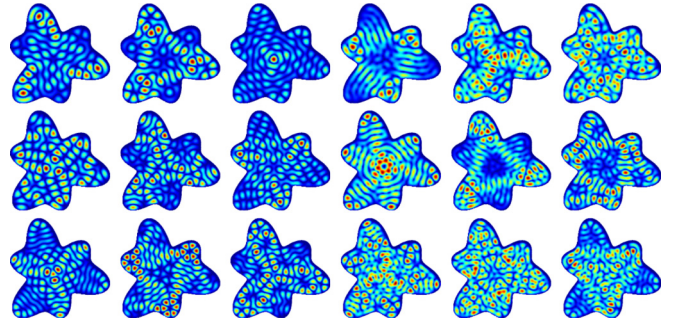

FIG. 3. Wave functions of the singlets (left three columns) and the corresponding doublets (right three columns) of the QB. They correspond to, from top left to bottom right in the left and right parts, eigenstates $\{k_n, \psi_n\}$ with $n = 34, 36, 39, 40, 51, 52, 55, 57, 58$. The color code goes from dark blue for zero intensity to red at the maximal intensity.

distributions of the massive NBs differ from the corresponding ones for the massless case. For the singlets the nodal line structure becomes discernible with increasing $\tilde{\beta}$ indicating that the wave functions become real [88]. Furthermore, the distributions of doublet partners approach each other with increasing $\tilde{\beta}$, as expected in the nonrelativistic limit. These features are visible in the local current shown in Figs. 7–9. It is defined as the expectation value of the current operator $\hat{u} = \nabla_p \hat{H}_D = c\hat{\sigma}$, $u(r) = c\psi^\dagger \hat{\sigma} \psi$. First, the local current can be used to test whether the BCs are fulfilled, that is, whether the outward current $n(s) \cdot u(s)$ vanishes along the boundary, which indeed is the case. In addition, the patterns exhibit a clear nodal-line pattern with increasing $\tilde{\beta}$. These observations may be explained by the fact that the wave-function components decouple and their patterns become similar. However, the second component becomes vanishingly small as compared to the first one with increasing $\tilde{\beta}$ [70]; see Eq. (38).

Figure 10 shows the nearest-neighbor spacing distribution $P(s)$, the integrated nearest-neighbor spacing distribution $I(s)$, the number variance $\Sigma^2(L)$, and the Dyson-Mehta statistic
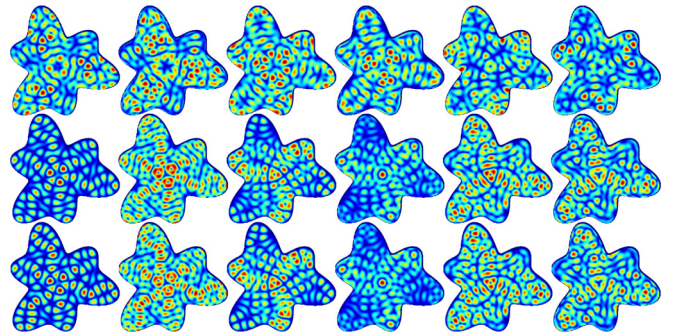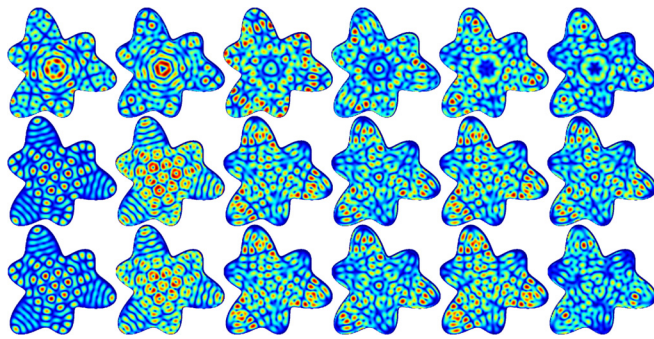

FIG. 4. Wave function intensity distributions of the first (first column) and second (second column) component of the singlets, the first (third column) and second (fourth column) component of the doublets with $l = 1$, and the first (fifth column) and second (sixth column) component of the doublets with $l = 2$ for $\tilde{\beta} = 0$ (first row), $\tilde{\beta} = 20$ (second row), and $\tilde{\beta} = 100$ (third row) for the eigenstate with $n = 45$. The color code goes from dark blue for zero intensity to red at the maximal intensity.

FIG. 5. Same as Fig. 4 for $n = 48$.

FIG. 7. Current corresponding to the wave functions shown in Fig. 4. The color code goes from dark blue for zero intensity to red at the maximal intensity.

$\Delta_3(L)$, which serves as a measure for the rigidity of a spectrum for the NBs with $\tilde{\beta} = 0, 20, 100$ and for the QB. For $\tilde{\beta} = 2$ the curves lie on top of those for $\tilde{\beta} = 0$. Before analyzing the fluctuation properties in the spectra we unfolded the eigenvalues $E_m = k_m^2$ to mean spacing unity. This was achieved for the QB and massless NB with Weyl's formula [89] by replacing the eigenvalues by $\epsilon_m = N^{\mathrm{Weyl}}(k_m)$ where for QBs $N^{\mathrm{Weyl}}(k_m) = \frac{\mathcal{A}}{4\pi}k_m^2 + \frac{\mathcal{L}}{4\pi}k_m + C_0$ with $\mathcal{A}$ denoting the area of the billiard and the perimeter contribution cancels out for NBs [68]. For the massive NBs unfolding was attained with a general second-order polynomial [44] which was fitted to the integrated spectral density. For the singlets, shown in the upper panel of Fig. 10, a transition from the GUE for the massless case to the GOE takes place when increasing the mass $\tilde{\beta}$ whereas for the doublets, shown in the lower panel, the curves are close to those of the GUE for all billiards. For the doublets, shown in the lower panel of Fig. 10, the curves are close to those of the GUE for all billiards. For $\tilde{\beta} = 100$ the spacing between the eigenvalues corresponding to $l = 1$ and $l = 2$, respectively, is much smaller than the average spacing in each subspectrum and the spectral properties of the NB are close to those of the QB when considering the same number of eigenvalues. Deviations from random matrix theory (RMT) predictions visible in the long-range correlations for the NB with mass $\tilde{\beta} = 100$ (orange squares), and also for the QB when taking into account only 1500 eigenvalues, are attributed to eigenstates localized along the shortest connected periodic orbit (PO) shown in Fig. 2 and along POs trapped in the bulges of the billiard visible in Fig. 3 and, e.g., in Fig. 5 for $\tilde{\beta} = 100$. These orbits are nontypical and analogous to the bouncing-ball orbits in the stadium billiard [90,91].
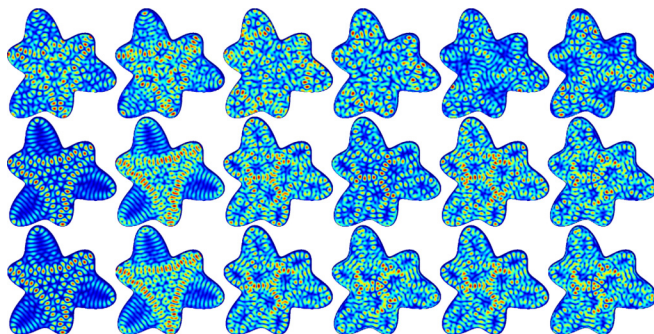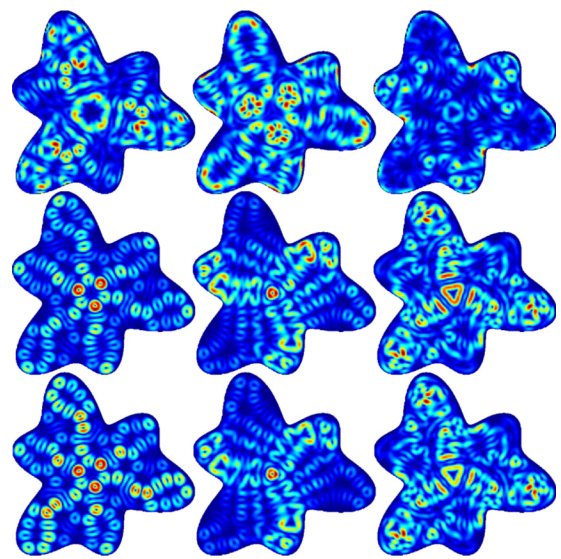
Their contributions lead to slow oscillations $N^{\mathrm{osc}}(k_m)$ in the fluctuating part of the integrated spectral density depicted as turquoise lines in Fig. 11. We removed their contributions to the spectral properties (cyan dots) by unfolding the eigenvalues with $\epsilon_m = N^{\mathrm{Weyl}}(k_m) + N^{\mathrm{osc}}(k_m)$ which, in addition to Weyl's formula, takes into account these oscillations [84,92]. Then the agreement with the spectral properties of the QB is very good.

The identification of slow oscillations is not an easy task, because it depends on the smoothing procedure and, in distinction from the determination of contributions from bouncing-ball orbits in the stadium billiard [91,92], the separation into fluctuating and oscillating contributions is not obvious. To determine the oscillating part we proceeded as
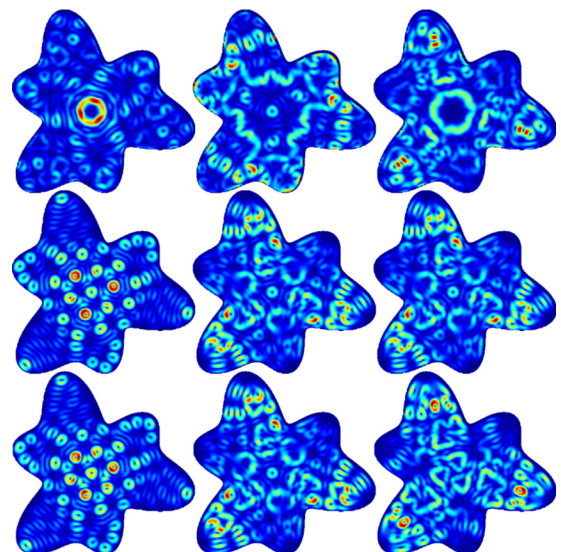

FIG. 6. Same as Fig. 4 for $n = 106$.

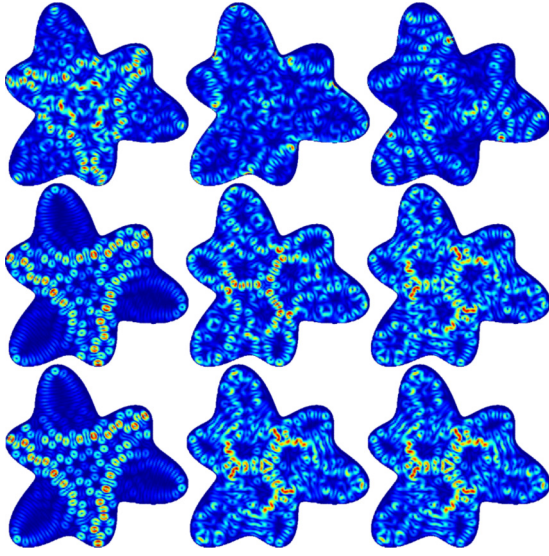FIG. 8. Current corresponding to the wave functions shown in Fig. 5.

FIG. 9. Current corresponding to the wave functions shown in Fig. 6.

in Ref. [84] and employed length spectra, which are obtained from the Fourier transform of the fluctuating part $\rho^{\mathrm{fluc}}(k)$ of the spectral density, $\rho(k) = \sum_m \delta(k - k_m)$, from wave number k to length l, $\tilde{\rho}(l) = |\int_0^{k_{\max}} dk e^{ikl} \rho^{\mathrm{fluc}}(k)|$, where l is shown in units of $r_0/3$. For nonrelativistic QBs the length spectra exhibit peaks at the lengths of the POs of the corresponding CB. In Fig. 12 we compare the length spectra of the QB and the NBs with $\tilde{\beta} = 0, 2, 20, 100$ deduced from the complete spectra including all eigenvalues irrespective of their transformation properties under rotation by $\frac{2\pi}{3}$. All length spectra exhibit peaks at the lengths of the POs of the CB, except that for the massless NB, peaks corresponding to POs with an odd number of reflections are missing [44], like, e.g., the shortest connected PO shown in Fig. 2. For the NB with $\tilde{\beta} = 2$ still some of the peaks are missing, however for $\tilde{\beta} = 20$ the length spectrum is already close to that of the QB and for $\tilde{\beta} = 100$ they are similar. Peaks at lengths smaller than the length of the shortest connected PO, $l_s = \tilde{l}_s/(r_0/3) = 11.336$, correspond to the POs trapped in the bulges. Accordingly, we determined $N^{\mathrm{osc}}(k_m)$ plotted as turquoise lines in Fig. 11 from the inverse Fourier transform of the length spectrum for lengths $l \leqslant l_s$ [84].

In Fig. 13 we compare the length spectra of the singlets ($l = 0$) and doublets ($l = 1, 2$) with those obtained from complete spectra for the QB and the NBs with $\tilde{\beta} = 0, 2, 20$. Only the length spectra of the singlets exhibit for sufficiently large $\tilde{\beta}$ a peak at the length of the shortest PO shown in Fig. 2. This explains why we observe largest deviations of the spectral properties from RMT predictions in their spectra. The length spectrum of the NB with $\tilde{\beta} = 20$ is similar to that of the QB and that of the NB with $\tilde{\beta} = 2$ to that of the massless NB. The symmetry-projected length spectra of the QB exhibit besides peaks at the lengths of the POs of the CB additional ones at the lengths of pseudo-orbits, which correspond to POs in the fundamental domain, but are not periodic when unfolded back to the full system. Yet, since these pseudo-orbits are POs of one of the fundamental domains, in the full system their initial
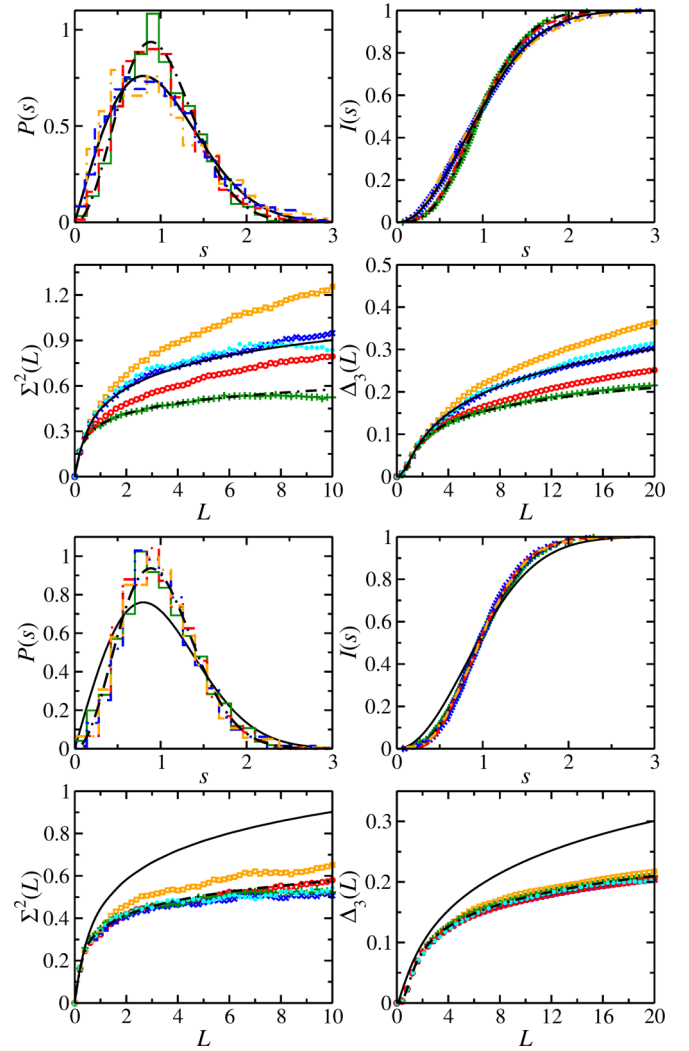

FIG. 10. Spectral properties of the singlets (top) and doublets (bottom) of the QB and NBs. Shown are the results for NBs with $\tilde{\beta} = 0$ (dark green lines and plus), $\tilde{\beta} = 2$ (dashed cyan lines and stars), $\tilde{\beta} = 20$ (dash-dotted red lines and circles), $\tilde{\beta} = 100$ before extraction of nongeneric contributions (orange dash-dot-dotted lines and circles) and afterward (cyan dots), and the QB (blue dash-dash-dotted lines and crosses). They are compared to the spectral properties of the GOE (black full line) and the GUE (dashed black line).

and final points are related via the symmetry operations of the associated irreducible representation [63,67]. Accordingly, the length spectra deduced from the symmetry-projected subspectra essentially correspond to those of quantum systems which are distinct from the full system. These features can be understood in terms of the symmetry-projected trace formula for QBs [63]. Also for the NBs the length spectra of the singlets and doublets exhibit peaks which are not observed in the complete spectra. In order to understand their appearance we extend the symmetry-projected trace formula for QBs to NBs, as outlined in Sec. II E.

E. Trace formula for threefold-symmetric neutrino billiards

The starting point for the derivation of the trace formulas were in Refs. [5,69,93] the underlying BIEs, Eqs. (19) with
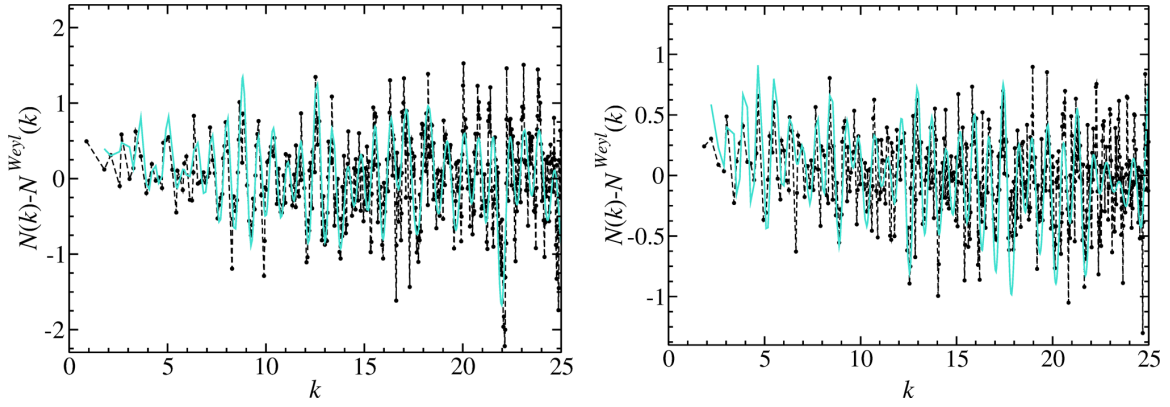
FIG. 11. Fluctuating part of the integrated spectral density (black dots and dashed lines) for the singlets (left) and doublets with $l = 1$ (right) and the slow oscillations (turquoise lines) resulting from nongeneric POs.

(20), (41) with (42), (31), and (47). These equations have nontrivial solutions at the zeros of the spectral determinant, leading to the quantization condition

$$\det(\mathbb{1} - \hat{\boldsymbol{Q}}^{(l)}(k)) = 0, \tag{51}$$

where $\hat{\boldsymbol{Q}}^{(l)}$ stands for $\hat{Q}^{QB(l)}$ defined in Eq. (15) or $\hat{\boldsymbol{Q}}^{NB(l)}$ given in Eq. (41). Accordingly, the integrated spectral density can be deduced from

$$N(k) = N^{\text{smooth}}(k) - \frac{1}{\pi} \lim_{\epsilon \to 0+} \text{Im} \ln \frac{\det[\mathbb{1} - \hat{Q}(k + i\epsilon)]}{\det[\mathbb{1} - \hat{Q}(0)]}, \tag{52}$$
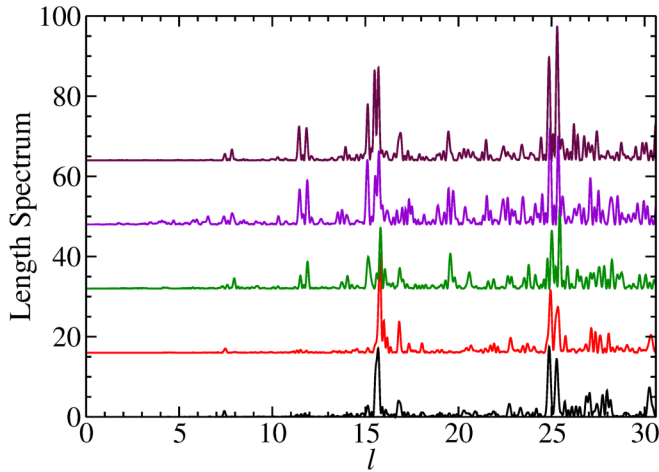
FIG. 12. Length spectra of the NBs for, from bottom to top, $\tilde{\beta} = 0$ (black), $\tilde{\beta} = 2$ (red), $\tilde{\beta} = 20$, $\tilde{\beta} = 100$ (violet), and the QB (maroon). Shown are the results for the complete spectra regardless of the symmetry properties of the eigenstates. For the massless NB the length spectrum exhibits no peaks at the lengths of POs with an odd number of reflections, some appear already for $\tilde{\beta} = 2$, for $\tilde{\beta} = 20$ the length spectrum exhibits peaks at the lengths of almost all POs, and for $\tilde{\beta} = 100$ it is similar to that of the QB. Here, and also in the other length spectra, l is given in units of $r_0/3$.

yielding for the spectral density [93,94]

$$\rho(k) = \rho^{\text{smooth}}(k) - \frac{1}{\pi} \text{Im} \frac{d}{dk} \ln \det[\mathbb{1} - \hat{\boldsymbol{Q}}^{(l)}(k)]$$

$$= \rho^{\text{smooth}}(k) + \frac{1}{\pi} \text{Im} \sum_{p=1}^{\infty} \frac{1}{p} \frac{d}{dk} [\text{Tr}(\hat{\boldsymbol{Q}}^{(l)})^p(k)], \tag{53}$$

with

$$\text{Tr}(\hat{\boldsymbol{Q}}^{(l)})^p(k) = \oint_{\partial\Omega} ds_1 \oint_{\partial\Omega} ds_2 \cdots \oint_{\partial\Omega} ds_p \mathcal{P}_p, \tag{54}$$

where $s_r = s(\phi_r)$ and $s_{p+1} = s_1$, $s_0 = s_p$. For the QB $\mathcal{P}_p$ is obtained from Eq. (20),

$$\mathcal{P}_p = \prod_{r=1}^{p} Q^{QB(l)}[k; \boldsymbol{r}(\phi_r), \boldsymbol{r}(\phi_{r+1})], \tag{55}$$

and for the massless NB from Eq. (43) with $\theta_\beta = 0$,

$$\mathcal{P}_p = 2 \cos\left(\sum_{r=1}^{p} \frac{\Delta\Phi(\phi_{r+1}, \phi_r)}{2}\right)$$

$$\times \prod_{r=1}^{p} Q_1^{NB(l); \tilde{\beta}=0}[k; \boldsymbol{r}(\phi_r), \boldsymbol{r}(\phi_{r+1})]. \tag{56}$$

For massive NBs a trace formula was derived in Ref. [69] on the basis of a combination of two BIEs, yielding a trace formula which interpolates between the ultrarelativistic and the nonrelativistic limit with minimized convergence problems. The corresponding product $\mathcal{P}_p$ is obtained by
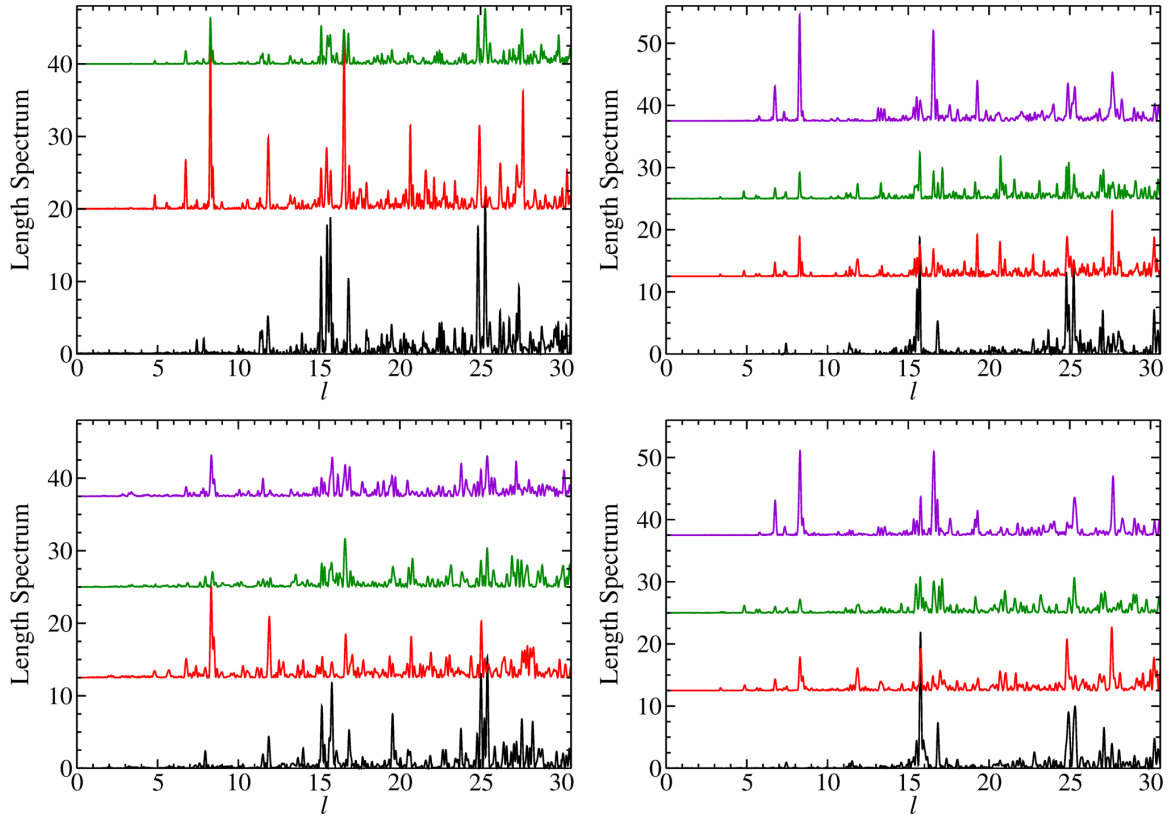
FIG. 13. Comparison of the length spectra of the QB (upper left), NB with $\tilde{\beta} = 0$ (upper right), $\tilde{\beta} = 20$ (lower left), and $\tilde{\beta} = 2$ (lower right) for, from bottom to top, the complete spectra (black) and the subspectra of the singlets with symmetry class $l = 0$ (red), and the doublet partners with symmetry classes $l = 1$ (dark green) and $l = 2$ (violet).

replacing $Q_1^{NB(l);\tilde{\beta}=0}$ in Eq. (56) with

$$
Q_1^{NB(l);\tilde{\beta}}[k; \boldsymbol{r}(\phi_r), \boldsymbol{r}(\phi_{r+1})]
$$

$$
= \cos\theta_\beta \left\{ \left[i\sin\left(\frac{\alpha_r - \alpha_{r+1}}{2}\right) - \sin\theta_\beta \cos\left(\frac{\alpha_r - \alpha_{r+1}}{2}\right) \right] H_0^{(1)}(k\rho) + \cos\theta_\beta \cos\left(\frac{\alpha_{r+1} + \alpha_r}{2} - \xi_{r+1,r}\right) H_1^{(1)}(k\rho) \right\}
$$

$$
+ \sin\theta_\beta \cos[\alpha_r - \xi_{r+1,r}] \left\{ \cos\theta_\beta \cos\left(\frac{\alpha_{r+1} + \alpha_r}{2} - \xi_{r+1,r}\right) H_0^{(1)}(k\rho) \right.
$$

$$
\left. - \left[i\sin\left(\frac{\alpha_r - \alpha_{r+1}}{2}\right) - \sin\theta_\beta \cos\left(\frac{\alpha_r - \alpha_{r+1}}{2}\right) \right] H_1^{(1)}(k\rho) \right\}. \tag{57}
$$

We use the abbreviations $\alpha_r = \alpha(\phi_r)$ and $\xi_{r+1,r} = \xi(\phi_{r+1}, \phi_r)$ which denote the angles of the outward-pointing normal vector at s_r and of the trajectory segment connecting the reflection points at s_r and s_{r+1} with respect to the x axis, respectively. To obtain the symmetry-projected trace formulas, we replace $Q = Q^{QB(l)}$, $Q_1^{NB(l)}$ with the sums Eqs. (32) or (48),

$$
\prod_{r=1}^{p} Q^{(l)}[k; \boldsymbol{r}(\phi_r), \boldsymbol{r}(\phi_{r+1})] = \prod_{r=1}^{p} \left\{ \sum_{\lambda=0}^{2} e^{i\frac{2l\pi}{3}\lambda} M_\lambda(k; \phi_r, \phi_{r+1}) \right\} = \sum_{\lambda=0}^{2} e^{i\frac{2l\pi}{3}\lambda} \mathcal{M}_\lambda^{p(l)}(k; \{\phi_i\}). \tag{58}
$$

We introduced

$$
\mathcal{M}_\lambda^{p(l)}(k; \{\phi_i\}) = \sum_{N_0=1}^{p} \sum_{N_1=1}^{p} \sum_{N_2=1}^{p} \hat{\delta}(N_0 + N_1 + N_2 - p) \hat{\delta}\left(\left\{ [N_1 + 2N_2] \frac{2\pi}{3} \right\} \text{modulo}(2\pi) - \lambda \right) \sum_{\{\pi_r\}} \prod_{r=1}^{N_0} M_0(k; \phi_{\pi_r}, \phi_{\pi_{r+1}})
$$

$$
\times \prod_{r=N_0+1}^{N_0+N_1} M_1(k; \phi_{\pi_r}, \phi_{\pi_{r+1}}) \prod_{r=N_0+N_1+1}^{p} M_2(k; \phi_{\pi_r}, \phi_{\pi_{r+1}}), \tag{59}
$$

where $\hat{\delta}(x)$ equals unity for $x = 0$ and zero otherwise and the sum over $\{\pi_r\} = \{\pi_1, \pi_2 \ldots, \pi_p\}$ is over all permutations π of $\{1, 2, \ldots, p\}$. The product is over angles from the first, second, or third domain in Fig. 2 for $N_0 = p$, $N_1 = p$, or $N_2 = p$, respectively, over angles from two subdomains when one of the N_i equals zero, and over the whole domain when none of the N_i vanishes.

The integrals Eq. (54) can be solved in the semiclassical limit $\hbar \to 0$ or $k \to \infty$ with $\hbar k$ fixed. For this we replace the Hankel functions by their asymptotic values for $k \to \infty$ [86] and extract them from $\mathcal{M}_\lambda^{p(l)}(k; \{\phi_i\})$, where we use the relation Eq. (16),

$$G_0[k; \boldsymbol{r}(\phi_r), \boldsymbol{r}(\phi_{r+1})] \simeq -\frac{i}{4} \sqrt{\frac{2}{\pi \rho_{r+1,r}}} e^{ik\rho_{r+1,r} - \frac{i}{4}\pi} \tag{60}$$

$$H_1(k\rho_{r+1,r}) \simeq \frac{1}{i} H_0(k\rho_{r+1,r}) \tag{61}$$

and

$$\partial_{n'} G_0[k; \boldsymbol{r}(\phi_r), \boldsymbol{r}(\phi_{r+1})] \simeq i \cos[\alpha_r - \xi_{r+1,r}] \cdot (-k) \cdot G_0[k; \boldsymbol{r}(\phi_r), \boldsymbol{r}(\phi_{r+1})]. \tag{62}$$

Inserting these asymptotic approximations of the Hankel functions into Eq. (59), in the semiclassical limit each of the summands of $\mathcal{M}_\lambda^{p(l)}(k; \{\phi_i\})$ in Eq. (59) can be split into a factor $\bar{\mathcal{M}}_\lambda^{p(l)}(\{\phi_i\})$, which does not depend on k and $\hbar$, and a product over normal derivatives of the Green's functions [5,69],

$$\text{Tr}(\hat{\boldsymbol{Q}}^{(l)})^p(k) \simeq \sum_{\lambda=0}^2 e^{i\frac{2l\pi}{3}\lambda} \sum_{N_0=1}^p \sum_{N_1=1}^p \sum_{N_2=1}^p \hat{\delta}(N_0 + N_1 + N_2 - p)\hat{\delta}\left(\left\{[N_1 + 2N_2]\frac{2\pi}{3}\right\}\text{modulo}(2\pi) - \lambda\right)$$

$$\times \sum_{\{\pi_r\}} \left(\frac{i}{2}\right)^p \frac{\bar{\mathcal{M}}_\lambda^{N_0,N_1,N_2}(\{\phi_{\pi_r}\})}{\prod_{r=1}^p \cos[\alpha_{\pi_r} - \xi_{\pi_{r+1},\pi_r}]} (-2)^p \sum_{\{\pi_r\}} \oint_{\partial\Omega} ds_1 \cdots \oint_{\partial\Omega} ds_p \prod_{r=1}^p \partial_{n_r} G_0[k; \boldsymbol{r}(s_{\pi_r}), \boldsymbol{r}(s_{\pi_{r+1}})]. \tag{63}$$

The p integrals can be performed by applying the stationary phase approximation [93] yielding that in the semiclassical limit the nonvanishing contributions to $\text{Tr}(\hat{\boldsymbol{Q}}^{(l)})^p(k)$ are POs of order p complying with the symmetry class l. Furthermore, the leading-k contribution to the derivative with respect to k in Eq. (54) comes from the phase factor resulting from the integrals over the normal derivatives of G_0. For the QB the second-last factor in Eq. (63) equals unity, and also for massless and massive NBs it neither depends on k nor on $\hbar$. The last term in Eq. (63) is the same as in the usual Gutzwiller trace formula for POs in the fundamental domain and we can use the results of Refs. [63,67,93] to obtain for the symmetry-projected trace formula

$$\text{Im}\frac{1}{p}\frac{d}{dk}[\text{Tr}(\hat{\boldsymbol{Q}}^{(l)})^p(k)] = \text{Re} \sum_{\gamma_p} \sum_{\lambda=0}^2 e^{i\frac{2l\pi}{3}\lambda} \cos\left(\Phi_{\gamma_p} - p\frac{\pi}{2}\right) \mathcal{B}_{\gamma_p}^{(l)\tilde{\beta}} e^{i\Gamma_{\gamma_p}^{(l)\tilde{\beta}}} \mathcal{A}_{\gamma_p}^{(l)} e^{i\Theta_{\gamma_p}^{(l)}}$$

$$+ \text{Re} \sum_{\gamma_p} \sum_{\lambda=0}^2 e^{i\frac{2l\pi}{3}\lambda} \cos\left(\Phi_{\gamma_p} + p\frac{\pi}{2}\right) \tilde{\mathcal{B}}_{\gamma_p}^{(l)\tilde{\beta}} e^{i\tilde{\Gamma}_{\gamma_p}^{(l)\tilde{\beta}}} \mathcal{A}_{\gamma_p}^{(l)} e^{i\Theta_{\gamma_p}^{(l)}}. \tag{64}$$

The sum over γ_p, that is, the sum over N_0, N_1, N_2 and the product in Eq. (63), is over all orbits which are periodic in the fundamental domain corresponding to the irreducible representation l. The second sum is obtained from the first one by reversing the direction of propagation of the POs. While for QBs both contributions are identical this is not the case for NBs [5,69]. Furthermore, $\mathcal{A}_{\gamma_p}^{(l)}$ and $\Theta_{\gamma_p}^{(l)}$ denote amplitudes and phases as in the usual Gutzwiller trace formula with

$$\mathcal{A}_{\gamma_p}^{(l)} = \frac{l_{\text{PO}}^{(p)}}{r_{\text{PO}}\sqrt{|\text{Tr}M_{\text{PO}}^{(p)} - 2|}}, \quad \Theta_{\gamma_p}^{(l)} = kl_{\text{PO}}^{(p)} - \frac{\pi}{2}\mu_{\text{PO}}^{(p)}. \tag{65}$$

Similarly, the amplitudes and phases of $\mathcal{B}_{\gamma_p}^{\tilde{\beta}} e^{i\Gamma_{\gamma_p}^{\tilde{\beta}}}$ coincide with those of the trace formula for massive NBs [69]. With

$$\chi_r = \xi_{r,r-1} - \alpha_r = \pi - (\xi_{r+1,r} - \alpha_r), \ 0 \leqslant \chi_r < \pi/2, \tag{66}$$

which gives the angle $\xi_{r,r-1}$ of $\boldsymbol{r}(\phi_r) - \boldsymbol{r}(\phi_{r-1})$ with respect to the angle α_r of the normal vector at s_r, we have with $\alpha_r - \alpha_{r+1} = \chi_{r+1} + \chi_r - \pi$ [69]

$$\Phi_{\gamma_p} = \sum_{r=1}^p \frac{\Delta\Phi(\phi_{r+1}, \phi_r)}{2} + p\frac{\pi}{2} = \sum_{r=1}^p \chi_r \tag{67}$$
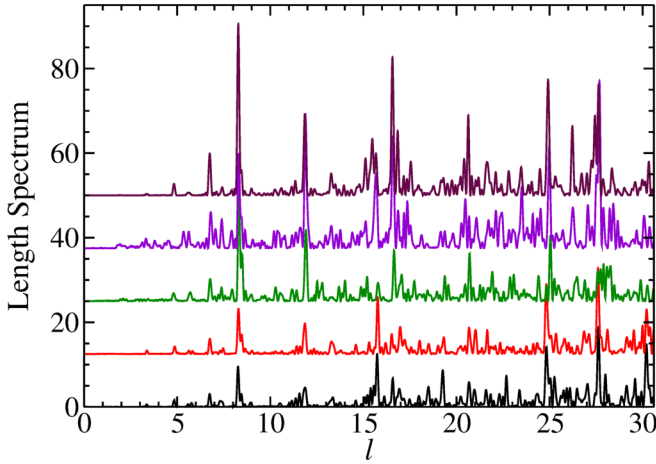
FIG. 14. Length spectra of the singlet states for, from bottom to top, the NBs with $\tilde{\beta} = 0$ (black), $\tilde{\beta} = 2$ (red), $\tilde{\beta} = 20$ (green), $\tilde{\beta} = 100$ (violet), and the QB (maroon).

and

$$
\mathcal{B}_{\gamma_p}^{\tilde{\beta}} e^{i\Gamma_{\gamma_p}^{\tilde{\beta}}} = \prod_{r=1}^{p} \left\{ i \sin\theta_\beta - \frac{\cos\theta_\beta}{\cos\chi_r} \right\}
$$
$$
\times \left[\cos\left(\frac{\chi_r + \chi_{r+1}}{2} \right) - i \sin\theta_\beta \sin\left(\frac{\chi_r + \chi_{r+1}}{2} \right) \right.
$$
$$
\left. + \cos\theta_\beta \sin\left(\frac{\chi_r - \chi_{r+1}}{2} \right) \right]. \tag{68}
$$

The product is over the reflection points r of orbits which are periodic in the fundamental domain corresponding to l. The factor $\tilde{\mathcal{B}}_{\gamma_p}^{\tilde{\beta}} e^{i\tilde{\Gamma}_{\gamma_p}^{\tilde{\beta}}}$ is obtained from Eq. (68) by reversing the signs of the angles χ_r and χ_{r+1}. The symmetry-projected trace formulas are sums over POs which are periodic in the respective fundamental domain, but not necessarily in the unfolded domain.

It has been shown in Ref. [69] that the additional factors as compared to the trace formula for QBs approach unity for

$\tilde{\beta} \to \infty$, yielding with Eq. (53)

$$
\rho^{\text{fluc}}(k; \tilde{\beta}) \xrightarrow{\tilde{\beta} \to \infty} \frac{1}{\pi} \text{Re} \sum_{\gamma_p} \sum_{\lambda=0}^{2} e^{i\frac{2l\pi}{3}\lambda} \mathcal{A}_{\gamma_p} e^{i\Theta_{\gamma_p}}, \tag{69}
$$

thus recovering the symmetry-projected trace formula for QBs [63,67]. In the ultrarelativistic limit we obtain

$$
\rho^{\text{fluc}}(k; \tilde{\beta}) \xrightarrow{\tilde{\beta} \to 0} \frac{1}{\pi} \text{Re} \sum_{\gamma_p} (-1)^p \cos\left(\Phi_{\gamma_p}\right) \cos\left(p\frac{\pi}{2}\right)
$$
$$
\times \sum_{\lambda=0}^{2} e^{i\frac{2l\pi}{3}\lambda} \mathcal{A}_{\gamma_p} e^{i\Theta_{\gamma_p}}. \tag{70}
$$

Summands with odd p vanish, implying that for $\tilde{\beta} = 0$ like in the full system only POs with an even number of reflections [44,73] contribute to the trace formula. This difference has its origin in the chirality property and the additional spin degree of freedom, i.e., the vectorial character of the Dirac equation [44,92,95]. Yet, for nonzero mass, i.e., $\theta_\beta \neq 0$, the additional phase factor Eq. (68) yields a nonvanishing contribution of POs with an odd number of reflections. Furthermore, due to this additional $\tilde{\beta}$-dependent phase factor the interference proceedings and thus the symmetry-projected length spectra may differ considerably from each other for the different symmetry classes and also from that of the full system.

Figures 14 and 15 exhibit the length spectra of the singlets and of the doublet partners with $l = 1$ (left) and $l = 2$ (right), respectively, for, from bottom to top, NBs with $\tilde{\beta} = 0, 2, 20, 100$ and the QB. Especially the length spectra of the doublets exhibit peaks for $\tilde{\beta} = 0$ which disappear with increasing mass. This is in contrast to the features of the full system, where peaks in the length spectra of the nonrelativistic QB exclusively disappear, namely those with an odd number of reflections, when decreasing $\tilde{\beta}$ to zero implying that the lengths associated with such peaks for $\tilde{\beta} = 0$ in the symmetry-projected length spectra correspond to those of pseudo-orbits. This behavior can be attributed to the additional $\tilde{\beta}$-dependent phase factor, which in the symmetry-projected trace formula leads to constructive instead of destructive interference at such peaks. The length spectra of the doublet partners are clearly distinguishable for $\tilde{\beta} = 0, 2, 20$, are close to each other for $\tilde{\beta} = 100$, and coincide for the QB. The origin of these features
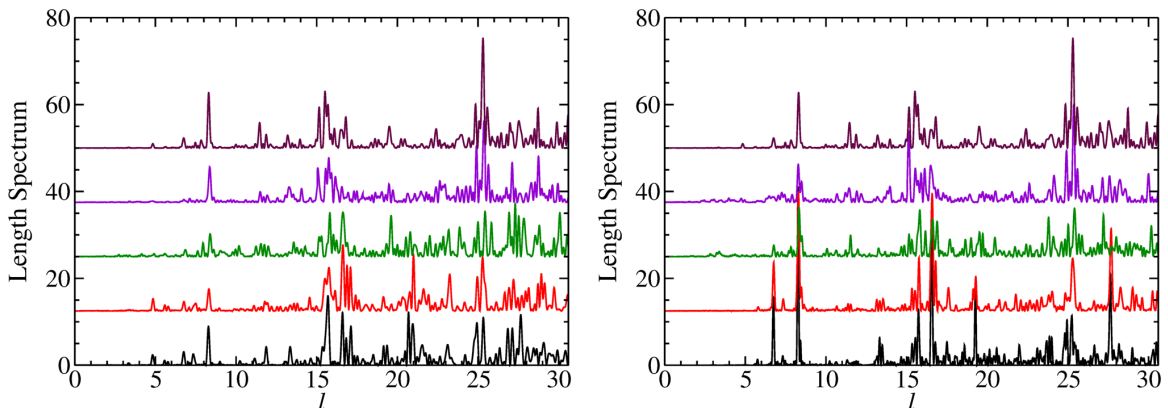

FIG. 15. Same as Fig. 14 for the doublets with $l = 1$ (left) and $l = 2$ (right).

again are the additional $\tilde{\beta}$-dependent factors, which depend on the direction of propagation of the POs, and thus differ for the doublets with $l = 1$ and $l = 2$ for finite $\tilde{\beta}$.

III. THE DIRAC BILLIARD WITH THREEFOLD SHAPE

We plan to do experiments with a microwave photonic crystal, that is, a DB [1] with shape Fig. 2 for the design shown in Fig. 1, described in detail in Sec. I. Like in the previous constructions of rectangular and Africa-shaped DBs [3,96] the cavity is constructed from a basin of 3 mm depth containing metallic cylinders arranged on a triangular grid, and a top plate. Both parts will be covered with lead and squeezed together tightly to achieve a superconducting resonator at liquid-helium temperature $T_{LH} = 4$ K. The cutoff frequency, below which the electric field strength excited in the cavity is perpendicular to the top and bottom plate, equals $f_{max} = 50$ GHz. The voids at the centers of respectively three adjacent cylinders form the corresponding GB (lower left inset), and the HB (lower right inset) corresponds to the combination of the kagome lattice formed by the centers between two adjacent cylinders and the honeycomb lattice [38]. The BCs are determined by the choice of the wall which passes through voids, implying Dirichlet BC at the corresponding sites in the HB and GB. Before starting with the construction of the DB, which currently takes at least a year, we performed numerical computations and compared these results with those for the relativistic and nonrelativistic QBs of Sec. II and for the GB and HB of corresponding shape presented in Sec. IV.

The eigenfrequencies and associated electric-field strengths, which are perpendicular to the top and bottom plate of the resonator, were obtained with COMSOL Multiphysics. Here we chose the value of r_0 in Eq. (2) as $r_0 = 30a_L/\sqrt{3}$ with $a_L = 12$ mm denoting the lattice constant, which is defined as the distance between the sites of the honeycomb lattice, i.e., the voids (lower left inset in Fig. 1) and the radius of the cylinders equaled $a_L/6$, yielding $N = 8890$ eigenmodes with eigenfrequencies f_m below 41 GHz. The DOS of the singlets and the doublets is similar. In Fig. 16 we show the DOS $\rho(f) = \sum_{m=1}^{N} \frac{\pi^2}{N} \delta(f - f_m)$ of the DB together with the smoothed DOS (black curve), which is obtained by replacing the δ functions by Lorentzians,

$$\rho^{smooth}(f) = \frac{\pi}{N} \sum_m \frac{\Gamma_L}{(f - f_m)^2 + \Gamma_L^2}, \quad (71)$$

where we chose $\Gamma_L = 0.075$. The DOS exhibits a Dirac point at ≈ 19 GHz and another one at ≈ 35 GHz, and van Hove singularities bordering them. They are separated by a broadened flat band of high spectral density. Note that at the frequencies of the van Hove singularities the DOS diverges logarithmically only for infinitely extended two-dimensional periodic lattice structures. We demonstrated in Ref. [2] that the peak height increases proportional to $N_c \ln N_c$, with N_c denoting the number of unit cells. At the flat band the eigenfrequencies are macroscopically degenerate in a perfect honeycomb-kagome lattice, whereas in the DB degeneracies are slightly lifted due to experimental imperfection and the overlap between wave function components located at the sites of the kagome lattice which corresponds to a coupling between these site. The val-
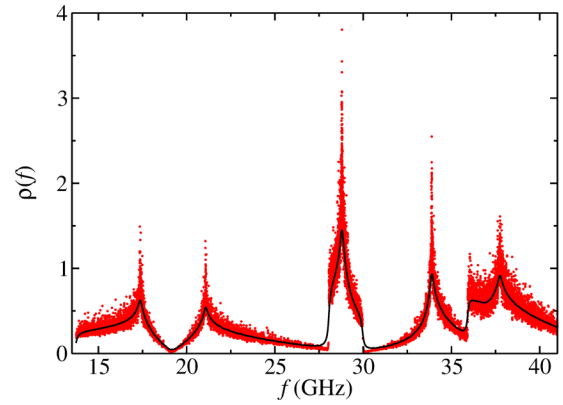

FIG. 16. Density of states of the DB. It exhibits Dirac points around $\simeq 19$ GHz and $\simeq 35$ GHz, which are framed by van Hove singularities. The associated bands are separated by a nearly flat band of exceptionally high spectral density. Above approximately the frequency of the upper Dirac point the DOS is distorted by adjacent bands of partly high spectral density.

ues of the hopping parameters of the appropriate graphene- or honeycomb-kagome-based TBM depend on the positions of the Dirac points, van Hove singularities, and flat band [3,33,38]. Around the upper Dirac point the DOS is distorted by an adjacent band leading to the excessive density, as seen in the two-dimensional band structure (dots) of the finite-size DB shown in Fig. 17. To obtain it we computed momentum distributions, that is, the Fourier transform of the electric field distributions, which in the considered frequency range correspond to the wave functions in the corresponding QB, from configurational space to quasimomentum space [3]. The locations of the maxima of the momentum distributions yield the values of the quasimomentum components $\mathbf{q} = (q_x, q_y)$ corresponding to the eigenfrequencies. The band structure is compared to that of an infinite-size array of metallic cylinders arranged on a triangular grid, shown in Ref. [3], which was
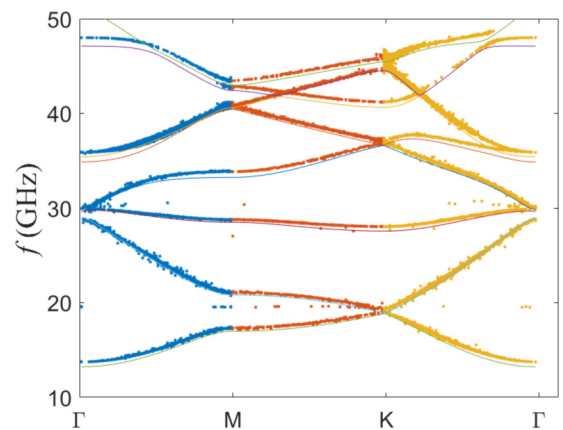

FIG. 17. Band structure function of the DB along a loop from the band edge (Γ point), to one of the saddle points (M points), corresponding to the van Hove singularities in the DOS, then to an adjacent Dirac point (K point) and back to the Γ point. The dots show the result for the DB (see main text), the lines that of an infinite-size array of metallic cylinders arranged on a triangular grid.
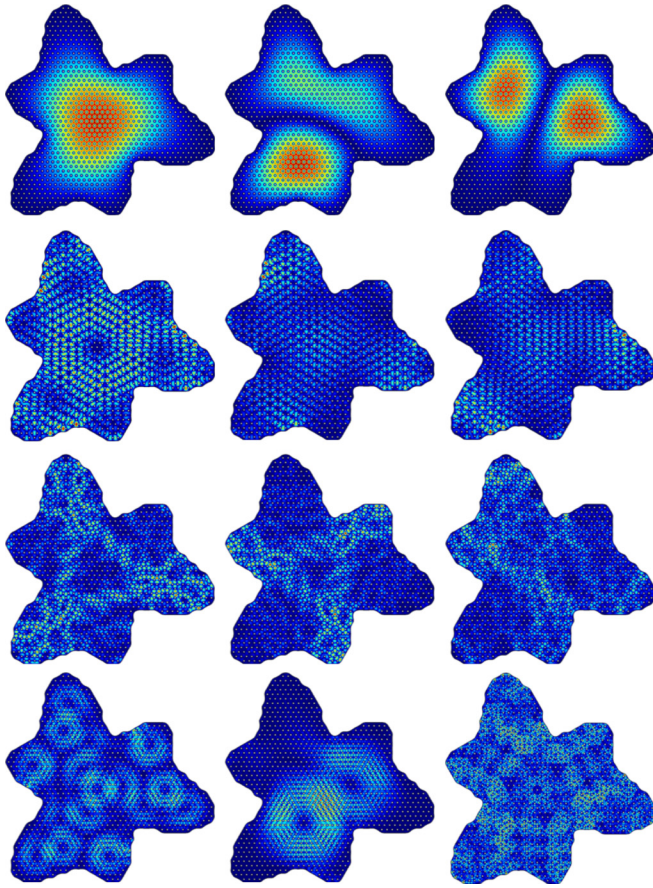
FIG. 18. Electric field intensity distributions of the DB from top left to bottom right corresponding to state numbers 1,2,3,996,1000,1001,1487,1512,1748,3092,3109,4071 below the flat band at the lower band edge (first row), around the Dirac point (second row), and around the upper band edge (third row). The bottom row shows one from the flat band, and above the flat band one around the lower band edge and one around the upper Dirac point. The color code goes from dark blue for zero intensity to red at the maximal intensity.
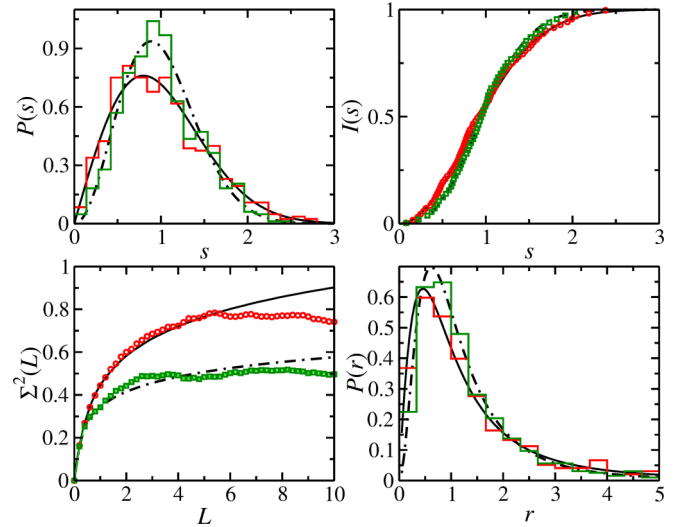

FIG. 19. Spectral properties of the singlets (red) and doublets (green) of the DB at the lower and upper band edge below the flat band. They are compared to the spectral properties of the GOE (black full line) and the GUE (dashed black line).

computed with the FEM [97] and shown to agree well with that of an infinitely extended honeycomb-kagome lattice in Ref. [38]. The frequency at which the band leading to deviations from the DOS of the corresponding HB occurs depends on the distance between the cylinders, which was chosen such that the number of propagating modes below the cutoff frequency f_{max} is as large as possible, implying that the distortion is unavoidable [38]. Note that the frequencies of propagating modes in the DB are identified with the eigenenergies in graphene [2]. As commonly done, the two-dimensional band structure is plotted along a loop in the quasimomentum plane from the band edge (Γ point) through one of the saddle points (M points) of the band structure, located at the frequencies of the van Hove singularities, and Dirac points (**K** points) and then back to Γ. Below the flat band and around it the band structure is similar to that of the rectangular DB [3,38], whereas above the upper Dirac point it is interwoven with a band emerging above $\simeq 41$ GHz.

In Fig. 18 we show typical examples for intensity distributions of the electric field strength, which in the considered

frequency range is perpendicular to the top and bottom plate of the resonator, so that they are identical to those of the wave functions of the corresponding QB, of the full system below the flat band in the region of the lower band edge (first row), the lower Dirac point (second row), and around the upper band edge (third row). In the fourth row we show one example in the flat band (left), and above the flat band, respectively, one around the lower band edge (middle) and the upper Dirac point (right). Counting from the upper left to the lower right distribution, the second and third and the fifth and sixth ones correspond to doublet partners. The associated wave functions are superpositions of the corresponding symmetry-projected states with $l = 1, 2$, and thus their intensity distributions differ. Due to rotational symmetry, the first, fourth, eighth, tenth, and twelfth ones can be unambiguously identified as singlets. In distinction to the rectangular HB, we already observe below the flat band localization of the electric field strength at the voids, which form the honeycomb sublattice, and of similar size between two neighboring cylinders, i.e., at the sites of the kagome lattice. Around the lowest band edge the wave functions are similar to the non-symmetry-projected ones of the QB. We will demonstrate in Sec. IV that, generally, below the flat band they are similar to those of the GB and HB, and above it to the HB, thus confirming the supposition of [38] for DBs with curved boundaries.

The eigenfrequency sequence can be separated into a subspectrum of singlets and two subspectra of degenerate doublets [56]. In cases where the identification of singlets and doublets was not unambiguous we checked the fluctuating part of the integrated density of the unfolded eigenfrequencies [85] and electric field intensity distributions. Here, we restricted ourselves to the region below the flat band comprising 670 eigenfrequencies for each symmetry class, because above the flat band an unambiguous classification of the eigenfrequencies into singlets and doublets was not possible. Note that in the experiments this is possible by using the method
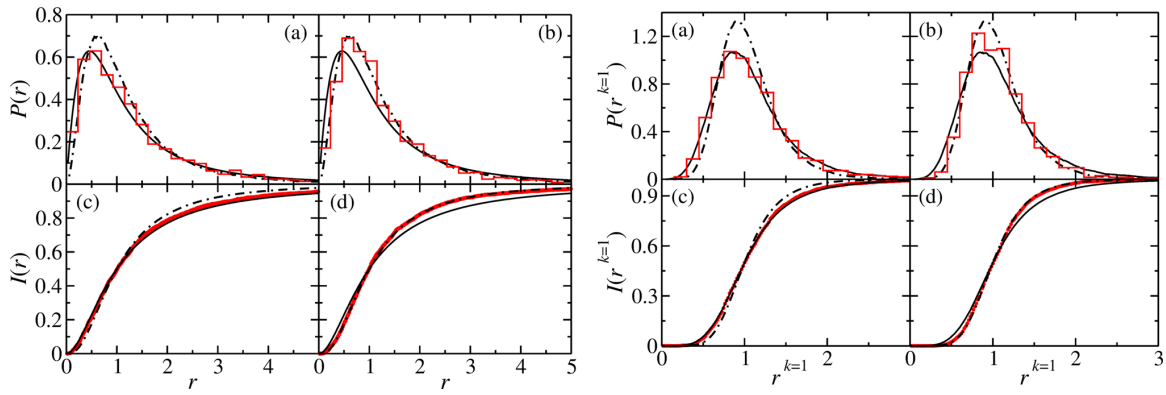
FIG. 20. Left: Ratio distributions [(a), (b)] and cumulative ratio distributions [(c), (d)] for the DB. The results for the singlets are shown in (a) and (c), those of the doublets in (b) and (d) (red). They are compared to those of the GOE (black full line) and the GUE (dashed black line). Agreement of the former with GOE and the latter with GUE is very good. Right: Same for the ($k = 1$)-overlapping ratio distributions and their cumulative distributions.

introduced in Ref. [60]. For the unfolding we ordered the eigenvalues by size, $f_i \leqslant f_{i+1}$, and shifted them such that $\tilde{f}_1 = 0$, $\tilde{f}_i = f_i - f_1$, and replaced $\tilde{f}_i$ by the smooth part of the integrated spectral density, $\epsilon_i = N^{\text{smooth}}(k_i)$ with k_i denoting the effective wave number. Note that the dispersion relation in a DB differs from that in a conventional billiard of corresponding shape, which does not contain any scatterers; namely, the frequencies depend quadratically on k_i around the band edges and linearly on k_i around the Dirac points. Accordingly, we define $k_i = \sqrt{|f_i - f_1|}$ with f_1 denoting the frequency at the respective band edge and $k_i = |f_i - f_1|$ with f_1 corresponding to the Dirac frequency [3], respectively. Then we can proceed as with QBs and determine $N^{\text{smooth}}(k_i)$ in both regions by fitting a second-order polynomial to $N(k_i)$. We analyzed the spectral properties using 250 singlets and doublets around the lower and around the upper band edge, respectively. In Fig. 19 we show the averages of the statistical measures for the singlets (red) and doublets (green). The former agree with the GOE curves; the latter are well described

by GUE statistics. Because of the small number of levels the agreement is not as good as, e.g., for the QB and NBs shown in Fig. 10. Below and above the Dirac point we have only around 125 eigenfrequencies in the region of linear dispersion. Therefore, we considered the distribution of the ratios [98,99] $r_i = \frac{\epsilon_{i+1} - \epsilon_i}{\epsilon_i - \epsilon_{i-1}}$ and the kth overlapping ratio distribution [100] of $r_i^k = \frac{\epsilon_{i+k+1} - \epsilon_i}{\epsilon_{i+k} - \epsilon_{i-1}}$ which are dimensionless so the non-unfolded eigenvalues can be used. It was demonstrated in Ref. [4,38] for rectangular and Africa-shaped GBs and rectangular HBs that they are applicable to the regions of van Hove singularities where the DOS exhibits a narrow peak. The results for the threefold DB are shown in Fig. 20. For the singlets the distributions agree well with those of the GOE; for the doublets they are well described by the GUE.

In Fig. 21 we show the length spectra for effective wave numbers k_i starting at the lower band edge, and in Fig. 22 for
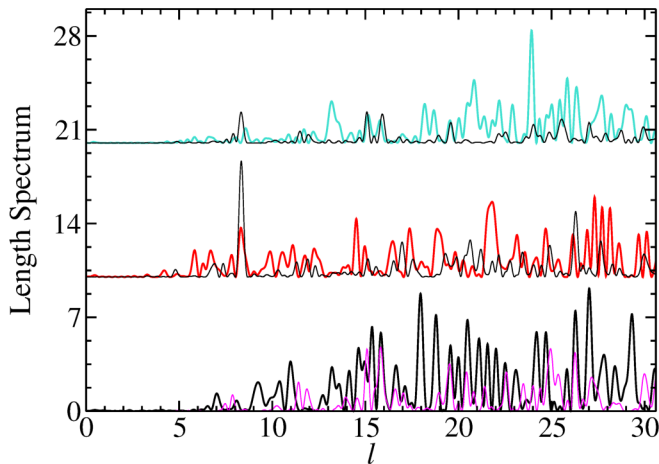

FIG. 21. Length spectra of the DB around the lower band edge for, from bottom to top, all eigenfrequencies irrespective of the symmetry class (black), the singlets (red), and the doublets (turquoise). They are compared to the corresponding length spectra of the QB (thin magenta and black lines) taking into account 250 levels.
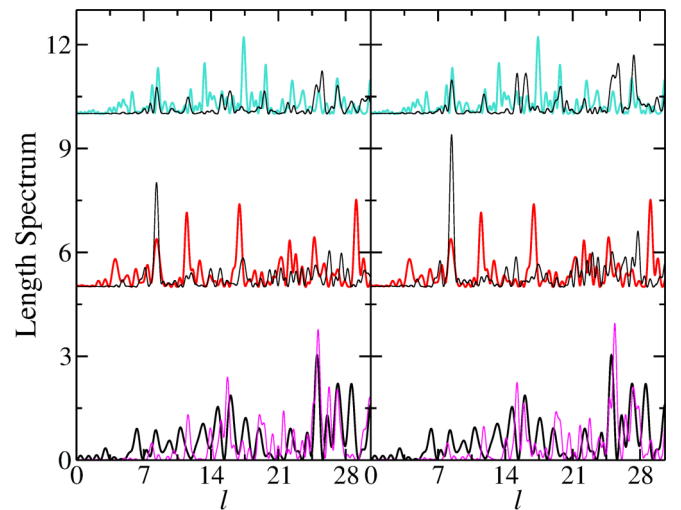

FIG. 22. Length spectra of the DB around the lower Dirac point (bold lines) compared with the length spectra of the QB (left) and NB with mass $\tilde{\beta} = 20$ (right) (thin lines), for, from bottom to top, all eigenfrequencies irrespective of the symmetry class (black, magenta), the singlets (red, black), and the doublets (turquoise, black), where we took into account 125 levels.
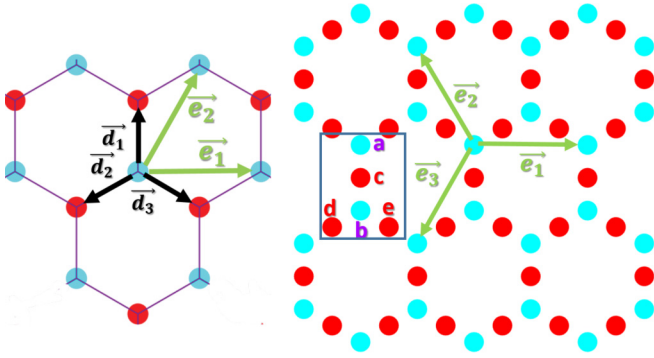
FIG. 23. Left: A honeycomb lattice consisting of three hexagonal cells is formed by two interpenetrating triangular sublattices (cyan and red disks, respectively). The unit cell of the honeycomb lattice consists of two sites, namely one of each sublattice. Right: A honeycomb-kagome lattice consisting of 8 hexagonal cells. The honeycomb-kagome lattice is formed by a honeycomb (red disks) and a kagome sublattice (cyan disks). The rectangular frame borders one unit cell of the kagome lattice.

k_i starting at the lower Dirac point, for, from bottom to top, the complete spectra (black), the singlets (red), and the doublets (turquoise). They are compared to the length spectra of the QB (thin lines) (left part in Fig. 22), where we used the number of eigenvalues equal to that of the available effective wave numbers k_i. Around the Dirac point we in addition compared the length spectra to those of the NB with mass $\tilde{\beta} = 20$ (right panel in Fig. 22). Generally, we find agreement in positions of peaks but not necessarily in height which can be attributed to the interference effects induced by the additional orbits in the DB. Their occurrence may be explained by the differing boundary shapes. As illustrated in Fig. 1, the boundary of the DB was chosen such that it passes through the honeycomb lattice sites framing the GB, which is formed by the voids in the DB, so that it has a rippled structure. Furthermore,

FIG. 25. Wave functions of the GB around the lower band edge for singlets (left three columns) and doublets (right three columns) corresponding to the wave functions of the QB shown in Fig. 3. The color code goes from dark blue for zero intensity to red at the maximal intensity.

when filling a QB with a curved boundary with a honeycomb lattice, there will be deviations between both structures along the boundary, and these lead to a loss of the analogy between the QB and GB for much lower state numbers than in a rectangular DB [3], as observed for the Africa-shaped DB [4]. Around the Dirac point, agreement of the length spectra of the DB with those of the NB with $\tilde{\beta} = 20$ is slightly better than with those of the QB, indicating that Robin BCs might be more appropriate than Dirichlet BCs to describe properties of the DB related to its void structure. We did not find any agreement with the length spectra of the massless NB.
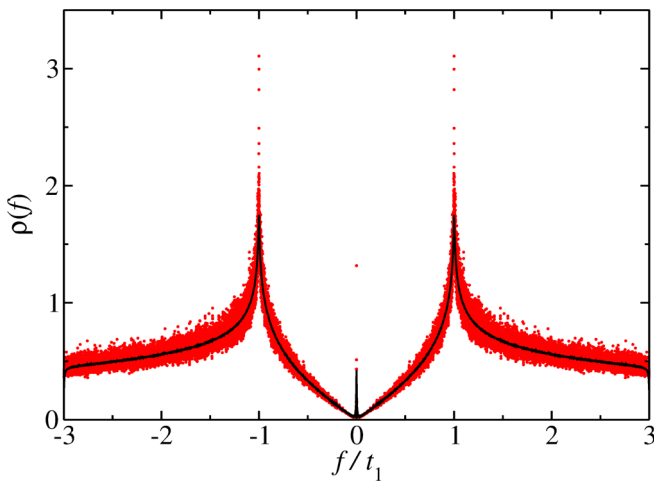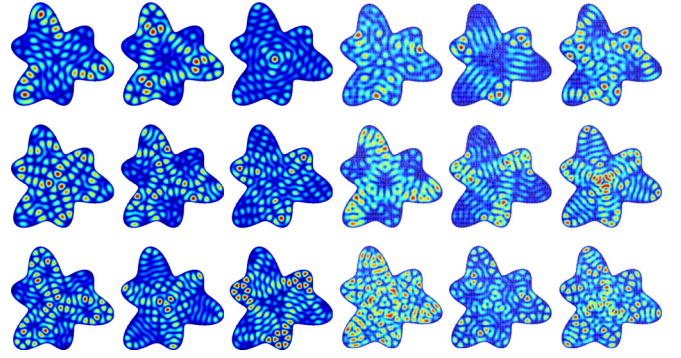

FIG. 24. Density of states of the singlets of the GB. It consists of $3N = 101\,835$ sites. The DOS (red dots) exhibits two van Hove singularities at $f = \pm t_1$ and a peak at the DP, which is due to the edge states that are localized at the zigzag edges of the GB. The black curve shows the smoothed DOS.
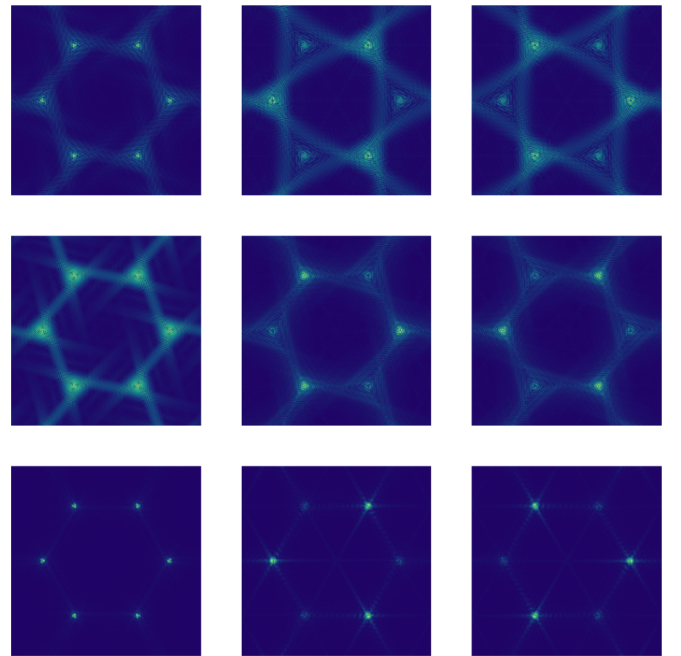

FIG. 26. Momentum distribution of the GB in the vicinity of the Dirac point for the singlets $l = 0$ (left part), and doublets with $l = 1$ (middle part) and $l = 2$ (right part). It is peaked on all six corners of the first Brillouin zone for $l = 0$, and on the three corners corresponding to one of the distinct Dirac points $\mathbf{K}_+$ and $\mathbf{K}_-$ associated with the triangular sublattices for $l = 1$ and $l = 2$, respectively.
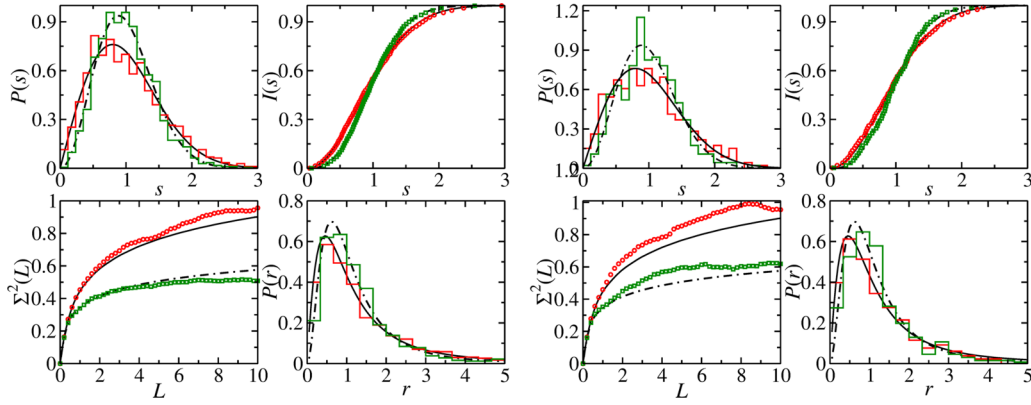
FIG. 27. Spectral properties of the GB around the lower band edge (left) and the Dirac point (right). For the singlets (red) they agree well with the GOE curves (black full lines), while those of the doublets (green) are well described by the GUE (black dash-dotted lines).

IV. GRAPHENE AND HONEYCOMB-KAGOME BILLIARDS WITH THREEFOLD SYMMETRY

The GB and HB were constructed by filling the subdomain 1 in Fig. 2 with a honeycomb or honeycomb-kagome lattice, respectively, and then rotating it twice by $\frac{2\pi}{3}$. The corresponding unit cells are shown in Fig. 23. A honeycomb lattice consisting of three hexagons is shown in the left part of Fig. 23. The hexagonal lattice is formed by two interpenetrating triangular sublattices (red and cyan dots). A unit cell generating the GB lattice consists of two adjacent sites, i.e., one site of each triangular sublattices. Subdomain 1 of the GB was generated with help of the translation vectors denoted by e_i, $i = 1, 2$. They are given in terms of the lattice constant a_L by

$$e_1 = a_L(1, 0), \quad e_2 = \frac{a_L}{2}(1, \sqrt{3}). \tag{72}$$

The distance vectors from the central site to next-nearest-neighbor sites equal

$$d_1 = \frac{a_L}{\sqrt{3}}(0, 1),$$

$$d_2 = -\frac{a_L}{2\sqrt{3}}\left(\sqrt{3}, \frac{1}{2}\right), \tag{73}$$

$$d_3 = \frac{a_L}{2\sqrt{3}}\left(\sqrt{3}, -\frac{1}{2}\right).$$

The right part of Fig. 23 shows a honeycomb-kagome lattice consisting of 8 hexagons. The corresponding unit cell is framed by a rectangle. Subdomain 1 of the HB was generated by employing the translation vectors marked by e_i, $i = 1, 2, 3$ [38],

$$e_1 = a_L(1, 0), \quad e_2 = \frac{a_L}{2}(-1, \sqrt{3}), \tag{74}$$

$$e_3 = -e_1 - e_2. \tag{75}$$

The distance vectors from site b to next-nearest-neighbor sites c, d, e are given by

$$d_1 = \frac{a_L}{2\sqrt{3}}(0, 1), \tag{76}$$

$$d_2 = -\frac{a_L}{4\sqrt{3}}\left(\sqrt{3}, \frac{1}{2}\right), \quad d_3 = \frac{a_L}{4\sqrt{3}}\left(\sqrt{3}, -\frac{1}{2}\right), \tag{77}$$

and from site c to neighboring ones a, b by

$$\tilde{d}_1 = \frac{a_L}{2\sqrt{3}}(1, 0), \quad \tilde{d}_2 = -\frac{a_L}{2\sqrt{3}}(1, 0). \tag{78}$$

We chose Dirichlet BCs on the sites adjacent to the boundary sites outside the billiard. To obtain the eigenvalues and wave functions of the GB and HB we used the TBM [3]. We chose equal on-site potentials for the GB ($t_0 = 0$) and the HB ($t_0 = 1$). Note that in Ref. [38] we chose different
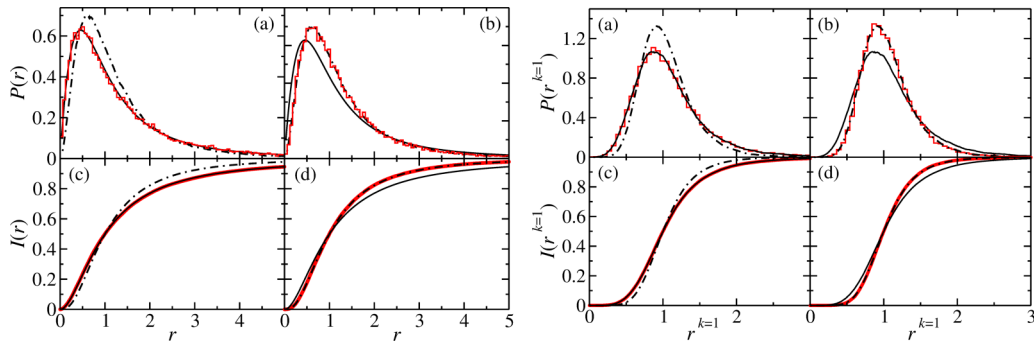

FIG. 28. Left: Ratio distributions [(a), (b)] and cumulative ratio distributions [(c), (d)] for the GB. The results for the singlets are shown in (a) and (c), those of the doublets in (b) and (d) (red). They are compared to those of the GOE (black full line) and the GUE (black dash-dotted line). Agreement of the former with GOE and the latter with GUE is very good. Right: Same for the ($k = 1$)-overlapping ratio distributions and their cumulative distributions.
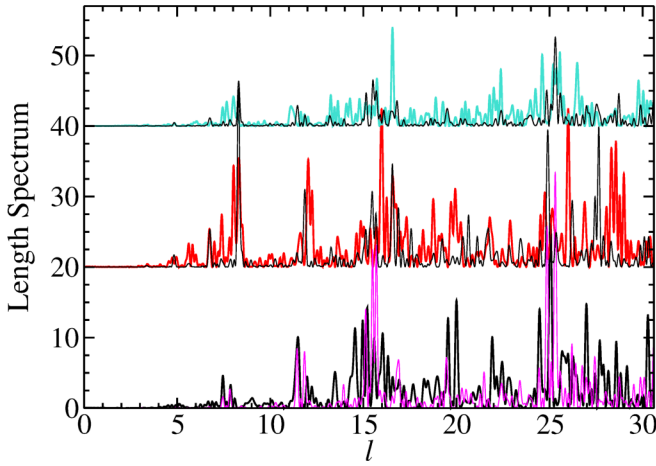
FIG. 29. Length spectra of the GB around the lower band edge for, from bottom to top, all eigenvalues (black), singlets (red), and doublets (turquoise) around the lower band edge (left) and Dirac point (right). They are compared to the corresponding length spectra of the QB (thin magenta and black lines) where we took into account the same number of levels, namely 800, as available for the GB.

values on the honeycomb and kagome sublattices to simulate a rectangular DB, of which the electric field distributions are predominantly localized at the voids, i.e., on the honeycomb sublattice, below the flat band. However, for DBs with the shape shown in Fig. 18 we observe similar localization at the voids and between two neighboring cylinders, that is, on the kagome sublattice. Furthermore, we considered only nearest-neighbor hoppings $t_1 = 3$, $t_2 = 0$ in the GB, and in the HB hoppings between the nearest-neighbor sites of the kagome and honeycomb sublattices, $t_1 = 1$, and in addition hoppings between nearest-neighbor sites of the kagome sublattice, $t_2 = 0.3$, to achieve a qualitative agreement of the DOS with that of the DB. For both the GBs and the HBs the entries
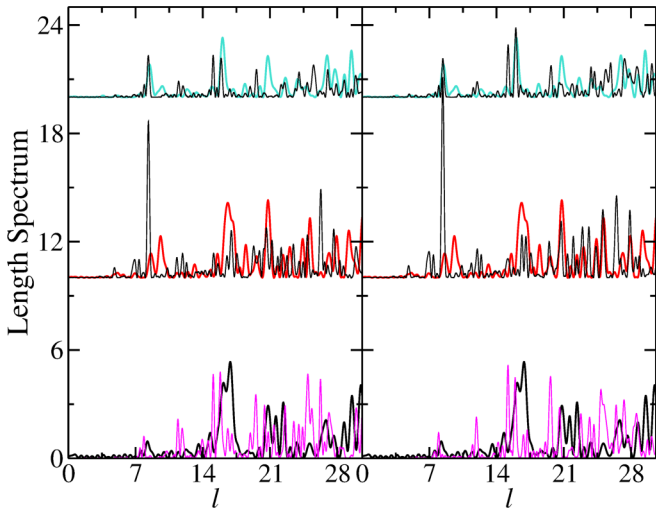

FIG. 30. Left: Same as Fig. 29 around the Dirac point, were we took into account 400 levels. Right: Same as left part, but the length spectra of the GB are compared with those of the NB with mass $\tilde{\beta} = 20$.
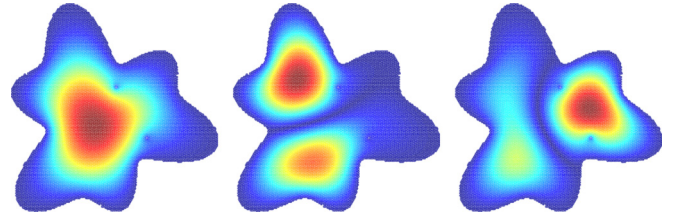

FIG. 31. The first eigenfunction of the singlet (left) and doublet states (middle, right) where 2 sites were removed to realize a GB with defects. The locations of the defects are recognizable as dark blue spots in the left and the right plot. The color code goes from dark blue for zero intensity to red at the maximal intensity.

of the TBM Hamiltonian matrix are obtained as

$$\hat{\mathcal{H}}_{ij}^{\text{TBM}} = t_0 \delta_{ij} + t_1 \hat{\delta}(|\mathbf{r}_i - \mathbf{r}_j| - d_0) + t_2 \hat{\delta}(|\mathbf{r}_i - \mathbf{r}_j| - d_1)$$

with $\mathbf{r}_i$ denoting the location of the sites i, $d_0 = a_L/\sqrt{3}$ for the honeycomb lattice, respectively, $d_0 = a_L/(2\sqrt{3})$ and $d_1 = a_L/2$ for the honeycomb-kagome lattice. The TBM Hamiltonian is $3N \times 3N$ dimensional if it comprises $3N$ sites and can be brought to the form

$$\hat{\mathcal{H}}_{\text{TBM}} = \begin{pmatrix} \hat{H} & \hat{V} & \hat{V}^T \\ \hat{V}^T & \hat{H} & \hat{V} \\ \hat{V} & \hat{V}^T & \hat{H} \end{pmatrix}. \tag{79}$$

Here, $\hat{H}$ refers to the N-dimensional Hamiltonian of each subdomain in Fig. 2. It comprises the on-site potentials and the next-nearest-neighbor hopping parameters. The $N \times N$ matrix $\hat{V}$ and its transposed $\hat{V}^T$ account for the coupling between two adjacent subdomains, that is, for the hoppings between the boundary sites along the common boundary.

The Hamiltonian has the same structure as the matrices $\hat{M}^{QB}$ in Eq. (28), the only difference being that their matrix entries are scalar, whereas in Eq. (79) they correspond to
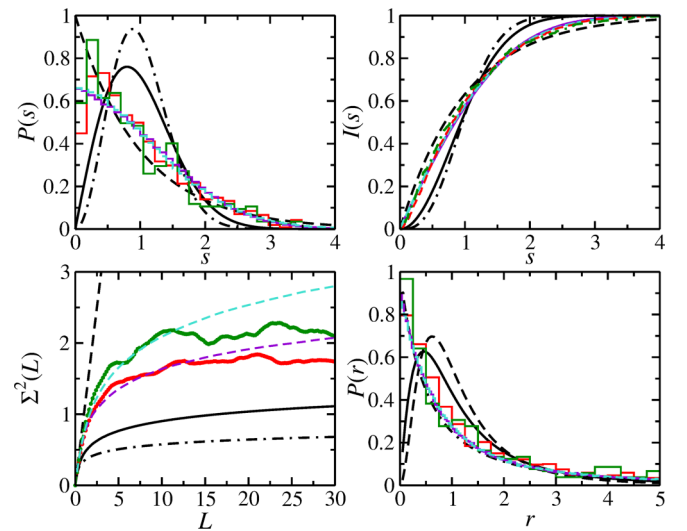

FIG. 32. Fluctuation properties in the complete eigenvalue spectrum of the GB with two defects (see Fig. 31) at the band edges (red) and the Dirac point (green). They are compared to the RMT results for a superposition of two GUEs and one GOE (violet dashed curves) and three GOEs (cyan dashed curves).
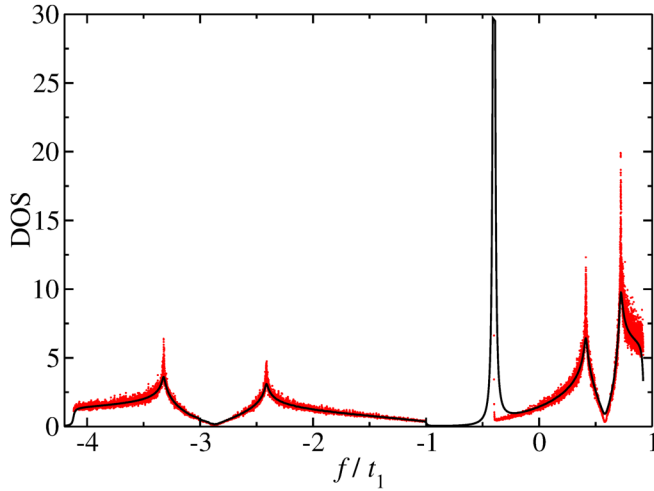
FIG. 33. Density of states (red) of the singlets of the HB, which consists of $3N = 15\,003$ lattice sites. It comprises two Dirac points bordered by van Hove singularities which are separated by a nearly flat band of exceptionally high density.

$N \times N$ matrices. Thus, by applying the matrix

$$\hat{U} = \frac{1}{\sqrt{3}} \begin{pmatrix} 1\!\!1_N & e^{i\frac{4\pi}{3}} 1\!\!1_N & e^{i\frac{4\pi}{3}} 1\!\!1_N \\ 1\!\!1_N & 1\!\!1_N & e^{i\frac{2\pi}{3}} 1\!\!1_N \\ 1\!\!1_N & e^{i\frac{2\pi}{3}} 1\!\!1_N & 1\!\!1_N \end{pmatrix}, \qquad (80)$$
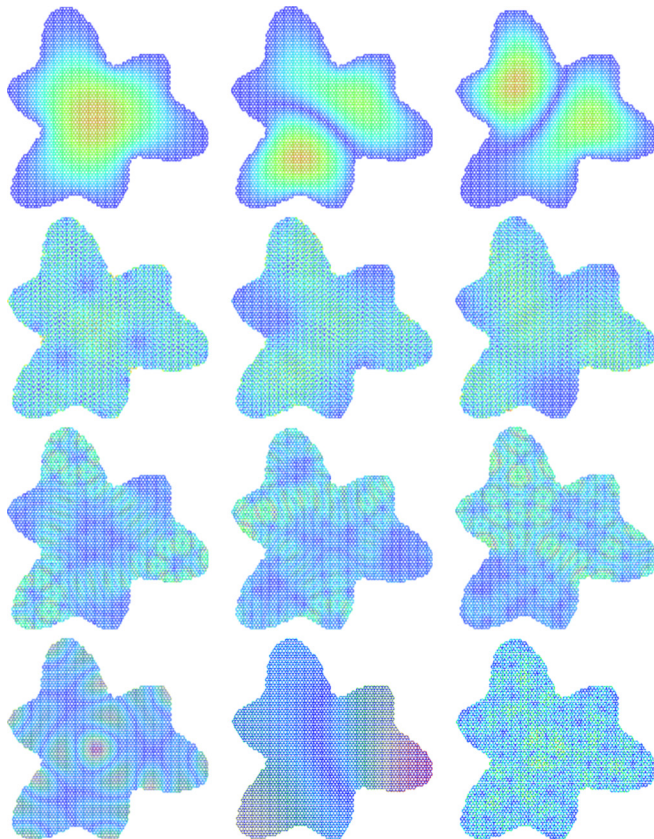

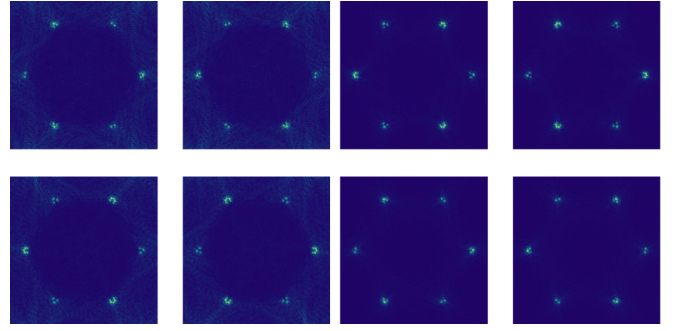FIG. 34. Same as Fig. 18 for the HB.

FIG. 35. Momentum distributions at the lower (left part) and upper (right part) Dirac point for the doublet partners with $l = 1$ (first column in each part) and $l = 2$ (second column in each part). Like in the GB they are selectively localized on the three corners of the first Brillouin zone corresponding to, respectively, one of the Dirac points $\mathbf{K}_+$ and $\mathbf{K}_-$.

with $1\!\!1_N$ denoting the N-dimensional unit matrix, the TBM Hamiltonian can be brought to block-diagonal form, where each block corresponds to one of the three irreducible symmetry classes labeled by $l = 0, 1, 2$,

$$\hat{U}^\dagger \hat{\mathcal{H}}_{TB} \hat{U} = \begin{pmatrix} \hat{H}^{TB(0)} & 0_N & \hat{0}_N \\ \hat{0}_N & \hat{H}^{TB(1)} & \hat{0}_N \\ \hat{0}_N & \hat{0}_N & \hat{H}^{TB(2)} \end{pmatrix},$$

$$\hat{H}^{TB(0)} = \hat{H} + \hat{V} + \hat{V}^T,$$

$$\hat{H}^{TB(1)} = \hat{H} + e^{i\frac{2\pi}{3}} \hat{V} + e^{i\frac{4\pi}{3}} \hat{V}^T,$$

$$\hat{H}^{TB(2)} = \hat{H} + e^{i\frac{4\pi}{3}} \hat{V} + e^{i\frac{2\pi}{3}} \hat{V}^T. \qquad (81)$$

The Hamiltonian $\hat{H}^{TB(0)}$ corresponding to eigenfunctions which are invariant under rotation by $\frac{2\pi}{3}$ is real symmetric and has nondegenerate eigenvalues, because the billiard does not exhibit any mirror symmetries, whereas $\hat{H}^{TB(1)}$ and $\hat{H}^{TB(2)}$ are complex Hermitian and complex conjugate to each other, $\hat{H}^{TB(1)} = (\hat{H}^{TB(2)})^*$. Accordingly, both have the same eigenvalues. Thus the spectrum of $\hat{\mathcal{H}}_{TB}$ consists of one subspectrum of singlets and two identical subspectra of doublets as in the QB.

For the GB we chose the lattice constant a_L such that a honeycomb lattice with $N = 33\,495$ sites fits into each subdomain and diagonalized the TBM Hamiltonian separately for each symmetry class. The resulting DOS of the singlets is shown in Fig. 24 (red dots) together with the smoothed DOS Eq. (71) (black line) where we chose $\Gamma_L = 0.01$. It is similar for all fundamental domains. In Fig. 25 we exhibit examples for wave functions of the GB around the lowest band edge. Agreement with corresponding ones of the QB is very good. However, this analogy between the QB and the GB is lost for eigenstate numbers $n \gtrsim 150$ where an increasing number of wave functions of the QB and GB differ due to the differences of their shapes at the curved boundary [4]. In the vicinity of the Dirac point they are localized at the zigzag edges of the boundary and vanish otherwise and at the van Hove singularities they are one-dimensional and localized along interior zigzag edges. Therefore, we do not show them. Yet, the momentum distributions corresponding to eigenstates close to the Dirac point exhibit interesting features. They are
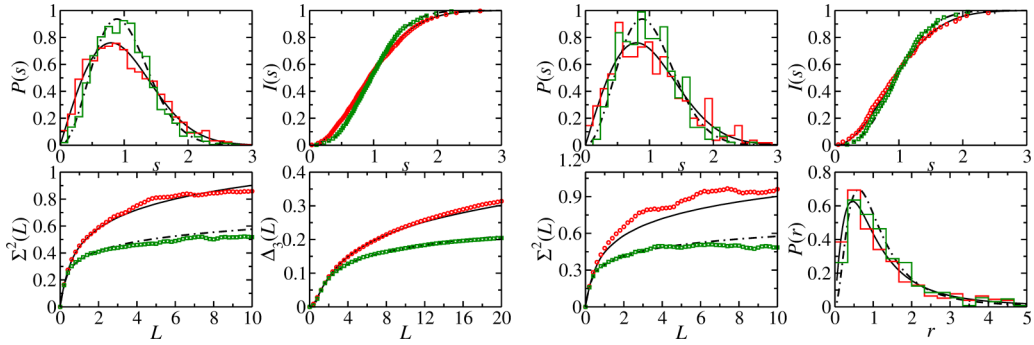
FIG. 36. Same as Fig. 27 for the HB. Shown is the superposition of the spectral properties around the lowest and uppermost band edge and around the lower and upper Dirac points.

obtained from the Fourier transform of the eigenfunctions from configurational space to quasimomentum space. Similar to the rectangular and Africa-shaped GBs [3,4,96], they are peaked at eigen-wave-vectors (k_x, k_y) of the corresponding QB close to the band edges, while in the vicinity of the van Hove singularities the momentum distributions are localized along the isoenergy lines connecting the saddle points of the band structure. In the vicinity of the Dirac point, the momentum distributions of the doublets are localized at respectively three corners of the first hexagonal Brillouin zone, i.e., on one of the two distinct Dirac points $\mathbf{K}_+$ and $\mathbf{K}_-$ associated with the two triangular sublattices, as clearly visible in Fig. 26. This is exactly the situation achieved in Refs. [76–80] in open phononic and sonic crystals, which were realized with rods arranged on a triangular grid like in the DB; however, the rods had a triangular instead of a circular cross section. Depending on the orientation of the triangles with respect to each other, a selective excitation of the valley states at the $\mathbf{K}_\pm$ Dirac points similar to the one in Fig. 26 was observed.

Figure 27 shows the spectral properties of the singlets (red) and doublets (turquoise) around the band edges (left) and the Dirac point (right), respectively. Since the DOS is symmetric with respect to the Dirac point we considered only eigenvalues at the lower band edge (1500 for each symmetry class) and above the Dirac point (400 for each symmetry class). We excluded edge states that correspond to wave functions localized at the zigzag parts of the boundary and lead to the peak in the DOS at the Dirac point. These would yield nonuniversal contributions and thus deviations from the RMT result. For the unfolding we ordered the eigenvalues by size, $E_i \leqslant E_{i+1}$,

shifted them such that $\tilde{E}_1 = 0$, and replaced them by the smooth part of the integrated spectral density, $\epsilon_i = N^{\text{smooth}}(k_i)$ with k_i denoting the effective wave numbers as outlined in Sec. III, $k_i = \sqrt{|E_i - E_{BE}|}$ at the band edge with $E = E_{BE}$ and $k_i = |E_i - E_{DP}|$ at the Dirac point with $E = E_{DP}$. The smooth part $N^{\text{smooth}}(k_i)$ was determined in both regions by fitting a second-order polynomial to $N(k_i)$ [3]. We find good agreement with GOE and GUE behavior for the singlets and doublets, respectively. Deviations are due to the POs trapped in the bulges of the GB and the shortest connected PO and decrease with increasing number of eigenvalues taken into account; see Sec. II D. In both regions the spectral properties coincide with those of the corresponding nonrelativistic QB and the DB, or the massive NB with mass $\tilde{\beta} \gtrsim 50$; see Fig. 1. In Fig. 28 we show results for the distribution of the ratios [98,99] and the kth overlapping ratio distribution [100] of the non-unfolded eigenvalues. Agreement with the GOE and GUE is very good for the singlets and doublets, respectively.

In Figs. 29 and 30 are shown the length spectra of the GB around the band edges and the Dirac point (bold lines), respectively. They are compared to the length spectra of the QB (left part in Fig. 30) and around the Dirac point also with those of the NB with $\tilde{\beta} = 20$ (right part in Fig. 30) (thin lines). Around the band edge the agreement is better for the full system and the singlets than for the doublets, concerning the positions of the peaks, whereas their heights generally deviate. Around the Dirac point the agreement of the length spectra of the GB with those of the QB and NB is similar. The occurrence of additional peaks and missing of others in the length spectra of the GB, especially for the singlets and doublets,
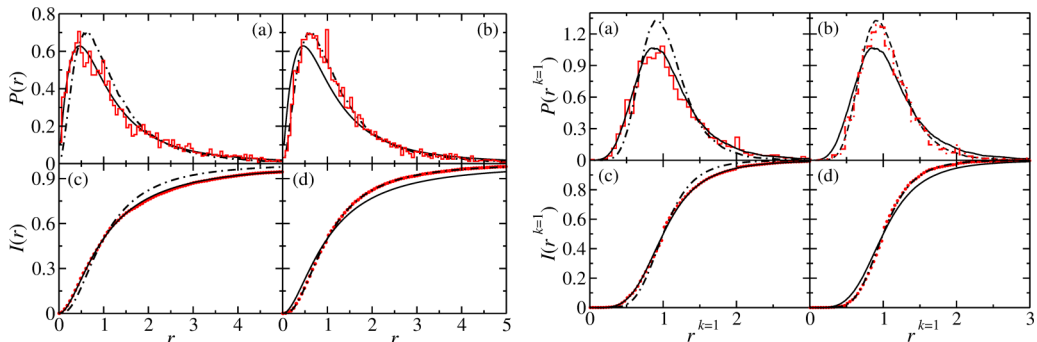

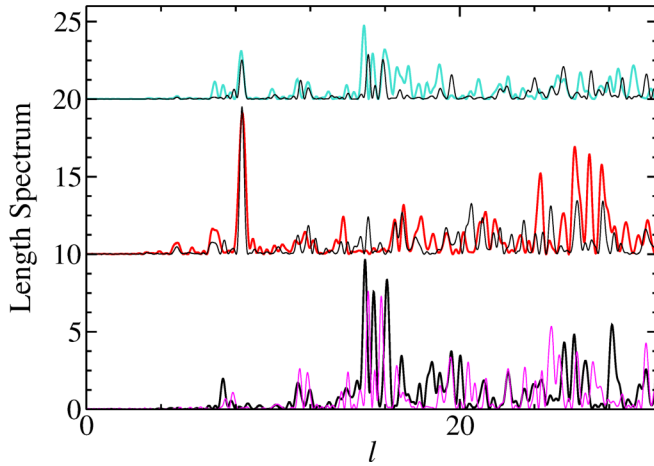
FIG. 37. Same as Fig. 28 for the HB.

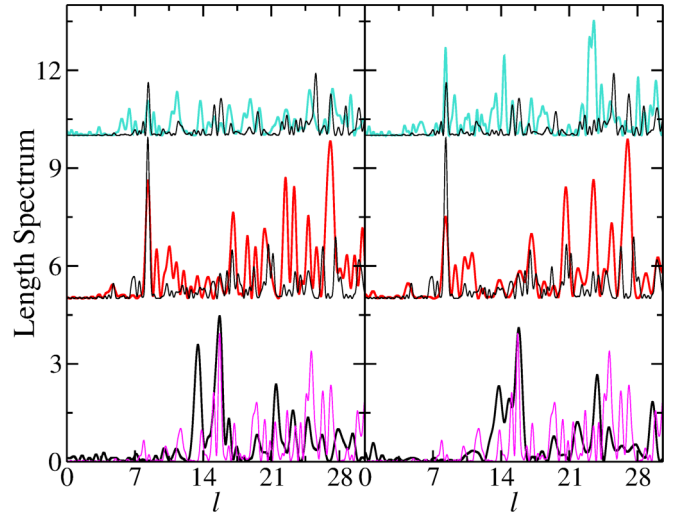FIG. 38. Same as Fig. 29 for the HB were we took into account 450 levels.

FIG. 39. Length spectra of the HB around the lower (left) and upper (right) Dirac point for, from bottom to top, all eigenvalues (black), singlets (red), and doublets (turquoise) compared to the corresponding length spectra of the QB (thin magenta and black lines) where we took into account in all cases 200 levels.

may be explained by the, due to the curved boundary, slightly differing shapes and BCs of the QB and GB; see Sec. III. Note that a trace formula was derived for GBs in Ref. [44] which can be brought to the symmetry-projected form by proceeding as in Sec. II E. Thus, also in the GB, peaks in the length spectra of the singlets and doublets that are not present in that of the full GB may be attributed to pseudo-orbits in the respective fundamental domain.

To study the effect of defects on the properties of the threefold GB we removed two sites from the honeycomb lattice. The locations are visible as blue spots in Fig. 31. The wave functions are distorted in the vicinity of the defects and the degeneracies of the doublet states are lifted. Thus, the spectrum cannot be divided into three subspectra. In Fig. 32 we show the fluctuation properties of the full system in the vicinity of the band edges (red) and the Dirac point (green). They are compared to those of block-diagonal random matrices, consisting of three equal-size blocks from the GOE (cyan dashed lines) or two blocks from the GUE and one block from the GOE. The latter would be applicable to a GB with threefold symmetry. The associated curves are barely distinguishable for the nearest-neighbor spacing distribution $P(s)$ and its cumulant $I(s)$ and for the ratio distribution $P(r)$. Yet, the long-range correlations are clearly distinguishable, as shown for the number variance $\Sigma^2(L)$. Interestingly, in the vicinity of the band edges the number variance agrees well with that for QBs with threefold symmetry and a chaotic classical dynamics, whereas in the vicinity of the Dirac point it agrees well with that of three GOE. Note that in the vicinity of the band edges the spectral properties coincide with those of a QB of corresponding shape, where the introduction of the two defects corresponds to a slight perturbation of the symmetry [101–103]. In the vicinity of the Dirac point, the lattice structure has a strong effect on the spectral properties of the GB, but it seemingly is still too weak to yield a complete coupling of the three blocks resulting from the irreducible representations, which would lead to agreement with one GOE.

For the HB we chose the lattice constant such that $N = 5001$ sites fit into each subdomain and again diagonalized the associated TBM separately for each symmetry class to obtain

the spectrum of the full HB. We also considered a larger HB with $N = 15\,453$ sites for the singlets and with $N = 9847$ sites for the doublets, respectively, to confirm the results obtained for $N = 5001$. The DOS is shown in Fig. 33 for the singlets and is similar for the doublets. It exhibits two Dirac points framed by van Hove singularities. These are separated by a nearly flat band of exceptionally high density. The hopping parameters were chosen such that the DOS qualitatively describes that of the DB introduced in Sec. III. The asymmetry is induced by the hopping between nearest-neighbor kagome lattice sites. Figure 34 exhibits examples for the wave functions of the HB. Corresponding wave functions of the DB are shown in Fig. 18 and, indeed, exhibit a similar pattern structure, thus confirming the results of Ref. [38]. In Fig. 35 we show examples of the momentum distributions of the doublet states $l = 1$ and $l = 2$ for two states at the lower (left) and upper (right) Dirac point. Pairs are localized selectively on either of the two Dirac points $\mathbf{K}_-$ and $\mathbf{K}_+$, respectively. Thus, the threefold-symmetric HB exhibits at both Dirac points the selectivity observed in the GB and in Refs. [76–80] for open phononic and sonic crystals.

The spectral properties are shown in Fig. 36. They were obtained from a superposition of the fluctuation properties of, respectively, 500 eigenvalues around the lower and upper band edges (red) and 200 eigenvalues below the lower and upper Dirac point (green). These and also the ratio distributions and $(k = 1)$-overlapping ratio distributions shown in Fig. 37 agree well with those of the corresponding QB, DB, and GB or the NB with $\tilde{\beta} \gtrsim 50$, i.e., with GOE for the singlets and with GUE for the doublets.

In Figs. 38–40 we show length spectra of the HB around the lower band edge and around the lower and upper Dirac point, respectively. They are compared to the length spectra of the QB (thin lines in Fig. 38 and in the left parts of Figs. 39 and 40). Around the band edge, agreement of the length spectra of the HB and QB is better than for the GB, especially for the
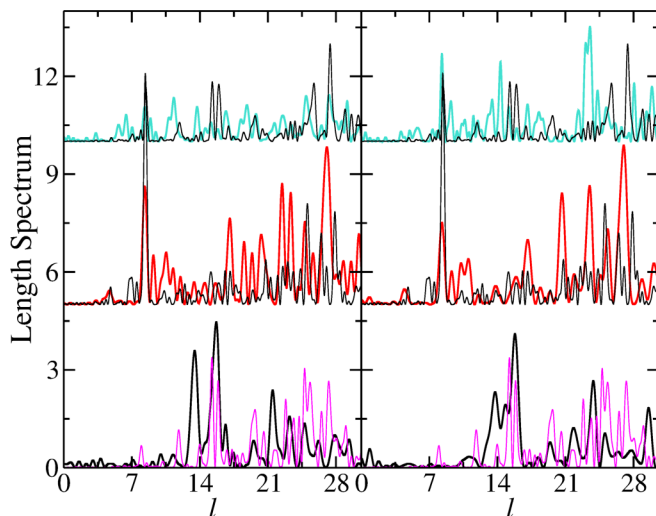
FIG. 40. Same as Fig. 39, but the length spectra are compared to those of the NB with $\tilde{\beta} = 20$.

singlets and doublets; that is, the QB reflects the properties in the fundamental domains better than those of the full system. Generally, the agreement between the length spectra of the HB with those of the QB and NB is comparable and better around the upper Dirac point than around the lower one.

V. CONCLUSIONS

We present a detailed study of the DOS, fluctuations in the spectra, and the wave functions of DBs, GBs, and HBs with a threefold-symmetric shape and compare them to those of QBs and NBs of various masses. We outline how the eigenstates of these billiards can be separated according to their transformation properties under rotation by $\frac{2\pi}{3}$ and computed for each fundamental domain 3000 eigenvalues and wave functions of the QB and the massless NB and 2000 of the massive NBs with mass $\tilde{\beta} = 0, 2, 20, 100$ and evaluated spectral properties and length spectra of the full system and in the symmetry-projected fundamental domains. It is known that the spectral properties of DBs, GBs, and also HBs deviate from those of NBs, because of the backscattering at their boundary which leads to a mixing of the valley states associated with the $\mathbf{K}_\pm$ points. Yet, in systems with threefold symmetry we observe a selective excitation of the valley states for the doublets. Still,

we find for the spectral properties agreement with those of the QB of corresponding shape, which implies that this selectivity is lost when departing from the Dirac point. We also investigated symmetry-projected length spectra. For small masses the doublet partners of the NBs exhibit clearly distinguishable length spectra; however, the eigenvalues of the DBs, GBs, and HBs corresponding to doublet partners are degenerate. Therefore, if at all, agreement can only be expected for massive NBs, as the associated singlets undergo a transition from GOE to GUE behavior and the doublet partners approach each other and their length spectra become similar with increasing $\tilde{\beta}$. We find agreement with the length spectra of QBs and also with those of NBs with $\tilde{\beta} = 20$, but we did not find any agreement of the length spectra of GBs and HBs with those of massless NBs, as predicted for GBs with infinite-mass confinement [44] based on a trace formula which, for circular billiards, has been shown to coincide with that of NBs [5]. These BCs best fit those of DBs; however, especially around the Dirac point, the properties of GBs and HBs sensitively depend on the structure of the boundary. The good agreement of the length spectra of the DB, GB, and HB with those of the NB with $\tilde{\beta} = 20$ indicates that Robin BCs, obeyed by NBs for sufficiently large mass, are appropriate for their description. Actually, a motivation for the study of length spectra and spectral properties of massive NBs is the search for BCs which yield a good description of those obtained experimentally with superconducting microwave billiards in Refs. [3,4] emulating artificial graphene and numerically for the DB with threefold symmetry. The experimental length spectra also exhibited deviations from those deduced based on the trace formula for graphene billiards with infinite-mass confinement [44]. We plan to perform experiments with a superconducting DB, which has the shape of the one presented in this paper. The eigenmodes can be separated into the three symmetry classes by proceeding as in Ref. [60]. Furthermore, we can slightly vary BCs and introduce defects for an in-depth study of their relation to QBs and massive NBs. Encouraged by the promising results for HBs, these studies will be accompanied by numerical simulations employing the honeycomb-kagome-lattice based TBM.

[1] S. Bittner, B. Dietz, M. Miski-Oglu, and A. Richter, Phys. Rev. B **85**, 064301 (2012).

[2] B. Dietz, F. Iachello, M. Miski-Oglu, N. Pietralla, A. Richter, L. von Smekal, and J. Wambach, Phys. Rev. B **88**, 104101 (2013).

[3] B. Dietz, T. Klaus, M. Miski-Oglu, and A. Richter, Phys. Rev. B **91**, 035411 (2015).

[4] B. Dietz, T. Klaus, M. Miski-Oglu, A. Richter, M. Wunderle, and C. Bouazza, Phys. Rev. Lett. **116**, 023901 (2016).

[5] B. Dietz and A. Richter, Phys. Scr. **94**, 014002 (2019).

[6] C. W. J. Beenakker, Rev. Mod. Phys. **80**, 1337 (2008).

[7] A. H. Castro Neto, F. Guinea, N. M. R. Peres, K. S. Novoselov, and A. K. Geim, Rev. Mod. Phys. **81**, 109 (2009).

[8] J. C. Slonczewski and P. R. Weiss, Phys. Rev. **109**, 272 (1958).

[9] D. P. DiVincenzo and E. J. Mele, Phys. Rev. B **29**, 1685 (1984).

[10] K. S. Novoselov, A. K. Geim, S. V. Morozov, D. Jiang, Y. Zhang, S. V. Dubonos, I. V. Grigorieva, and A. A. Firsov, Science **306**, 666 (2004).

[11] A. Geim and K. Novoselov, Nat. Mater. **6**, 183 (2007).

[12] P. Avouris, Z. Chen, and V. Perebeinos, Nat. Nanotechnol. **2**, 605 (2007).

[13] F. Miao, S. Wijeratne, Y. Zhang, U. C. Coskun, W. Bao, and C. N. Lau, Science **317**, 1530 (2007).

[14] L. A. Ponomarenko, F. Schedin, M. I. Katsnelson, R. Yang, E. W. Hill, K. S. Novoselov, and A. K. Geim, Science **320**, 5874 (2008).

[15] X. Zhang and Z. Liu, Phys. Rev. Lett. **101**, 264303 (2008).

[16] D. Abergel, V. Apalkov, J. Berashevich, K. Ziegler, and T. Chakraborty, Adv. Phys. **59**, 261 (2010).

[17] S. R. Zandbergen and M. J. A. de Dood, Phys. Rev. Lett. **104**, 043903 (2010).

[18] M. Polini, F. Guinea, M. Lewenstein, H. C. Manoharan, and V. Pellegrini, Nat. Nanotechnol. **8**, 625 (2013).

[19] P. V. Parimi, W. T. Lu, P. Vodo, J. Sokoloff, J. S. Derov, and S. Sridhar, Phys. Rev. Lett. **92**, 127401 (2004).

[20] S. Joannopoulos, J. D. Johnson, R. Meade, and J. Winn, *Photonic Crystals: Molding the Flow of Light* (Princeton University Press, Princeton, 2008).

[21] A. Singha, M. Gibertini, B. Karmakar, S. Yuan, M. Polini, G. Vignale, M. I. Katsnelson, A. Pinczuk, L. N. Pfeiffer, K. W. West, and V. Pellegrini, Science **332**, 1176 (2011).

[22] L. Nádvorník, M. Orlita, N. A. Goncharuk, L. Smrčka, V. Novák, V. Jurka, K. Hruška, Z. Výborný, Z. R. Wasilewski, M. Potemski, and K. Výborný, New J. Phys. **14**, 053002 (2012).

[23] K. K. Gomes, W. Mar, W. Ko, F. Guinea, and H. C. Manoharan, Nature (London) **483**, 306 (2012).

[24] L. Tarruell, D. Greif, T. Uehlinger, G. Jotzu, and T. Esslinger, Nature (London) **483**, 302 (2012).

[25] T. Uehlinger, G. Jotzu, M. Messer, D. Greif, W. Hofstetter, U. Bissbort, and T. Esslinger, Phys. Rev. Lett. **111**, 185307 (2013).

[26] S. Bittner, B. Dietz, M. Miski-Oglu, P. Oria Iriarte, A. Richter, and F. Schäfer, Phys. Rev. B **82**, 014301 (2010).

[27] U. Kuhl, S. Barkhofen, T. Tudorovskiy, H.-J. Stöckmann, T. Hossain, L. de Forges de Parny, and F. Mortessagne, Phys. Rev. B **82**, 094308 (2010).

[28] M. C. Rechtsman, Y. Plotnik, J. M. Zeuner, D. Song, Z. Chen, A. Szameit, and M. Segev, Phys. Rev. Lett. **111**, 103901 (2013).

[29] M. C. Rechtsman, J. M. Zeuner, A. Tünnermann, S. Nolte, M. Segev, and A. Szameit, Nat. Photonics **7**, 153 (2013).

[30] A. B. Khanikaev, S. H. Mousavi, W.-K. Tse, M. Kargarian, A. H. MacDonald, and G. Shvets, Nat. Mater. **12**, 233 (2013).

[31] X. Wang, H. T. Jiang, C. Yan, F. S. Deng, Y. Sun, Y. H. Li, Y. L. Shi, and H. Chen, Europhys. Lett. **108**, 14002 (2014).

[32] Z. Shi, L. Gan, T.-H. Xiao, H.-L. Guo, and Z.-Y. Li, ACS Photonics **2**, 1513 (2015).

[33] S. Reich, J. Maultzsch, C. Thomsen, and P. Ordejón, Phys. Rev. B **66**, 035412 (2002).

[34] T. Jacqmin, I. Carusotto, I. Sagnes, M. Abbarchi, D. D. Solnyshkov, G. Malpuech, E. Galopin, A. Lemaître, J. Bloch, and A. Amo, Phys. Rev. Lett. **112**, 116402 (2014).

[35] Z. Lan, N. Goldman, and P. Öhberg, Phys. Rev. B **85**, 155451 (2012).

[36] J.-L. Lu, W. Luo, X.-Y. Li, S.-Q. Yang, J.-X. Cao, X.-G. Gong, and H.-J. Xiang, Chin. Phys. Lett. **34**, 057302 (2017).

[37] H. Zhong, Y. Zhang, Y. Zhu, D. Zhang, C. Li, Y. Zhang, F. Li, M. R. Belić, and M. Xiao, Ann. Phys. **529**, 1600258 (2017).

[38] W. Maimaiti, B. Dietz, and A. Andreanov, Phys. Rev. B **102**, 214301 (2020).

[39] P. G. Silvestrov and K. B. Efetov, Phys. Rev. Lett. **98**, 016802 (2007).

[40] F. Libisch, C. Stampfer, and J. Burgdörfer, Phys. Rev. B **79**, 115423 (2009).

[41] J. Wurm, A. Rycerz, İ. Adagideli, M. Wimmer, K. Richter, and H. U. Baranger, Phys. Rev. Lett. **102**, 056806 (2009).

[42] L. Huang, Y.-C. Lai, D. K. Ferry, S. M. Goodnick, and R. Akis, Phys. Rev. Lett. **103**, 054101 (2009).

[43] L. Huang, Y.-C. Lai, and C. Grebogi, Phys. Rev. E **81**, 055203(R) (2010).

[44] J. Wurm, K. Richter, and İ. Adagideli, Phys. Rev. B **84**, 075468 (2011).

[45] A. Rycerz, Phys. Rev. B **85**, 245424 (2012).

[46] A. Rycerz, Phys. Rev. B **87**, 195431 (2013).

[47] L. Huang, H.-Y. Xu, C. Grebogi, and Y.-C. Lai, Phys. Rep. **753**, 1 (2018).

[48] M. Bellec, U. Kuhl, G. Montambaux, and F. Mortessagne, Phys. Rev. Lett. **110**, 033902 (2013).

[49] M. Bellec, U. Kuhl, G. Montambaux, and F. Mortessagne, Phys. Rev. B **88**, 115437 (2013).

[50] M. Bellec, U. Kuhl, G. Montambaux, and F. Mortessagne, New J. Phys. **16**, 113023 (2014).

[51] M. V. Berry and M. Tabor, J. Phys. A **10**, 371 (1977).

[52] M. Berry, *Structural Stability in Physics* (Pergamon Press, Berlin, 1979).

[53] G. Casati, F. Valz-Gris, and I. Guarnieri, Lett. Nuovo Cimento **28**, 279 (1980).

[54] O. Bohigas, M. J. Giannoni, and C. Schmit, Phys. Rev. Lett. **52**, 1 (1984).

[55] M. L. Mehta, *Random Matrices* (Academic Press, London, 1990).

[56] F. Leyvraz, C. Schmit, and T. H. Seligman, J. Phys. A **29**, L575 (1996).

[57] J. P. Keating and J. M. Robbins, J. Phys. A: Math. Gen. **30**, L177 (1997).

[58] P. B. F. Leyvraz and T. H. Seligman, New J. Phys. **13**, 063027 (2011).

[59] C. Dembowski, H.-D. Gräf, A. Heine, H. Rehfeld, A. Richter, and C. Schmit, Phys. Rev. E **62**, R4516 (2000).

[60] C. Dembowski, B. Dietz, H.-D. Gräf, A. Heine, F. Leyvraz, M. Miski-Oglu, A. Richter, and T. H. Seligman, Phys. Rev. Lett. **90**, 014102 (2003).

[61] M. C. Gutzwiller, J. Math. Phys. **12**, 343 (1971).

[62] M. C. Gutzwiller, *Chaos in Classical and Quantum Mechanics* (Springer, Berlin, 1990).

[63] J. M. Robbins, Phys. Rev. A **40**, 2128 (1989).

[64] S. C. Creagh and R. G. Littlejohn, Phys. Rev. A **44**, 836 (1991).

[65] S. C. Creagh and R. G. Littlejohn, J. Phys. A: Math. Gen. **25**, 1643 (1992).

[66] T. H. Seligman and H. A. Weidenmüller, J. Phys. A **27**, 7915 (1994).

[67] C. H. Joyner, S. Müller, and M. Sieber, J. Phys. A **45**, 205102 (2012).

[68] M. V. Berry and R. J. Mondragon, Proc. R. Soc. London A **412**, 53 (1987).

[69] B. Dietz and Z.-Y. Li, Phys. Rev. E **102**, 042214 (2020).

[70] G. Baym, *Lectures on Quantum Mechanics* (CRC Press, Boca Raton, FL, 2018).

[71] W. A. Gaddah, J. Phys. A: Math. Theor. **51**, 385304 (2018).

[72] M.-Y. Song, Z.-Y. Li, H.-Y. Xu, L. Huang, and Y.-C. Lai, Phys. Rev. Res. **1**, 033008 (2019).

[73] J. Bolte and S. Keppeler, Ann. Phys. **274**, 125 (1999).

[74] S. Keppeler, Ann. Phys. **304**, 40 (2003).

[75] P. Carmier and D. Ullmo, Phys. Rev. B **77**, 245413 (2008).

[76] J. Lu, C. Qiu, S. Xu, Y. Ye, M. Ke, and Z. Liu, Phys. Rev. B **89**, 134302 (2014).

[77] J. Lu, C. Qiu, M. Ke, and Z. Liu, Phys. Rev. Lett. **116**, 093901 (2016).

[78] J. Lu, C. Qiu, L. Ye, X. Fan, M. Ke, F. Zhang, and Z. Liu, Nat. Phys. **13**, 369 (2017).

[79] L. Ye, C. Qiu, J. Lu, X. Wen, Y. Shen, M. Ke, F. Zhang, and Z. Liu, Phys. Rev. B **95**, 174106 (2017).

[80] B.-Z. Xia, T.-T. Liu, G.-L. Huang, H.-Q. Dai, J.-R. Jiao, X.-G. Zang, D.-J. Yu, S.-J. Zheng, and J. Liu, Phys. Rev. B **96**, 094106 (2017).

[81] B. Dietz and U. Smilansky, Chaos **3**, 581 (1993).

[82] F. Haake, S. Gnutzmann, and M. Kuś, *Quantum Signatures of Chaos* (Springer, Heidelberg, 2018).

[83] R. Schäfer, M. Barth, F. Leyvraz, M. Müller, T. H. Seligman, and H.-J. Stöckmann, Phys. Rev. E **66**, 016202 (2002).

[84] B. Dietz, A. Heine, V. Heuveline, and A. Richter, Phys. Rev. E **71**, 026703 (2005).

[85] A. Bäcker, *Numerical Aspects of Eigenvalue and Eigenfunction Computations for Chaotic Quantum Systems* (Springer, Berlin, 2003), pp. 91–144.

[86] M. Abramowitz and I. A. Stegun, editors, *Handbook of Mathematical Functions with Formulas, Graphs, and Mathematical Tables* (Dover, New York, 2013).

[87] P. Yu, B. Dietz, and L. Huang, New J. Phys. **21**, 073039 (2019).

[88] P. Yu, B. Dietz, H.-Y. Xu, L. Ying, L. Huang, and Y.-C. Lai, Phys. Rev. E **101**, 032215 (2020).

[89] H. Weyl, J. Reine Angew. Math. **141**, 1 (1912).

[90] M. V. Berry, Proc. R. Soc. London A **400**, 229 (1985).

[91] M. Sieber, U. Smilansky, S. C. Creagh, and R. G. Littlejohn, J. Phys. A **26**, 6217 (1993).

[92] C. Dembowski, B. Dietz, H.-D. Gräf, A. Heine, T. Papenbrock, A. Richter, and C. Richter, Phys. Rev. Lett. **89**, 064101 (2002).

[93] M. Sieber, J. Phys. A **30**, 4563 (1997).

[94] M. Sieber, Nonlinearity **11**, 1607 (1998).

[95] R. Balian and B. Duplantier, Ann. Phys. (NY) **104**, 300 (1977).

[96] B. Dietz, F. Iachello, and M. Macek, Crystals **7**, 246 (2017).

[97] E. I. Smirnova, C. Chen, M. Shapiro, J. Sirigiri, and R. Temkin, J. Appl. Phys. **91**, 960 (2002).

[98] V. Oganesyan and D. A. Huse, Phys. Rev. B **75**, 155111 (2007).

[99] Y. Y. Atas, E. Bogomolny, O. Giraud, and G. Roux, Phys. Rev. Lett. **110**, 084101 (2013).

[100] Y. Atas, E. Bogomolny, O. Giraud, P. Vivo, and E. Vivo, J. Phys. A **46**, 355204 (2013).

[101] C. Ellegaard, T. Guhr, K. Lindemann, J. Nygård, and M. Oxborrow, Phys. Rev. Lett. **77**, 4918 (1996).

[102] H. Alt, C. I. Barbosa, H.-D. Gräf, T. Guhr, H. L. Harney, R. Hofferbert, H. Rehfeld, and A. Richter, Phys. Rev. Lett. **81**, 4847 (1998).

[103] B. Dietz, A. Heine, A. Richter, O. Bohigas, and P. Leboeuf, Phys. Rev. E **73**, 035201(R) (2006).